Key Points:
- Novel ocean observations reveal the detailed evolution between upper ocean salinity and temperature during Irma's rapid intensification (RI)
- The rate of change of θ_E caused solely by surface fluxes was sufficient to support atmospheric boundary layer recovery during RI over the river plume
- Theoretical frameworks highlight how perturbing the vertical salinity gradient influences tropical cyclone intensity and intensification

Supporting Information:
- Supporting Information S1

Correspondence to:
J. E. Rudzin,
johna.rudzin.ctr@nrlmry.navy.mil

Author Contributions:
Data curation: Elizabeth R. Sanabia, Steven R. Jayne
Funding acquisition: Sue Chen, Elizabeth R. Sanabia, Steven R. Jayne
Methodology: Sue Chen
Project administration: Sue Chen, Elizabeth R. Sanabia, Steven R. Jayne
(continued)

The Air-Sea Response During Hurricane Irma's (2017) Rapid Intensification Over the Amazon-Orinoco River Plume as Measured by Atmospheric and Oceanic Observations

Johna E. Rudzin[1,2] iD, Sue Chen[2] iD, Elizabeth R. Sanabia[3] iD, and Steven R. Jayne[4] iD

[1]National Research Council, U.S. Naval Research Laboratory, Monterey, CA, USA, [2]Marine Meteorology Division, U.S. Naval Research Laboratory, Monterey, CA, USA, [3]Oceanography Department, U.S. Naval Academy, Annapolis, MD, USA, [4]Physical Oceanography Department, Woods Hole Oceanographic Institute, Woods Hole, MA, USA

Abstract Hurricane Irma (2017) underwent rapid intensification (RI) while passing over the Amazon-Orinoco River plume in the tropical Atlantic. The freshwater discharge from the plume creates a vertical salinity gradient that suppresses turbulent heat flux from the cool, ocean subsurface. The stability within the plume reduces sea surface temperature (SST) cooling and promotes energetic air-sea fluxes. Hence, it is hypothesized that this ocean feature may have facilitated Irma's RI through favorable upper ocean conditions. This hypothesis is validated using a collection of atmospheric and oceanic observations to quantify how the ocean response influences surface flux and atmospheric boundary layer thermodynamics during Hurricane Irma's RI over the river plume. Novel aircraft-deployed oceanic profiling floats highlight the detailed evolution of the ocean response during Irma's passage over the river plume. Analyses include quantifying the ocean response and identifying how it influenced atmospheric boundary layer temperature, moisture, and equivalent potential temperature (θ_E). An atmospheric boundary layer recovery analysis indicates that surface fluxes were sufficient to support the enhanced boundary layer θ_E (moist entropy) observed, which promotes inner-core convection and facilitates TC intensification. The implicit influence of salinity stratification on Irma's intensity during RI is assessed using theoretical intensity frameworks. Overall, the findings suggest that the salinity stratification sustained SST during Irma's passage, which promoted energetic air-sea fluxes that aided in boundary layer recovery and facilitated Irma's intensity during RI. Examination of the air-sea coupling over this river plume, corresponding atmospheric boundary layer response, and feedback on TC intensity was previously absent in literature.

1. Introduction

Hurricane Irma (2017) was one of the most powerful Atlantic hurricanes, sustaining Category 5 strength winds (≥137 kt) for an unprecedented 60 hr. The TC attained such strength early on in its life cycle when it rapidly intensified (RI ~ 30 kt increase in 24 hr) to 155 kt by 5 September 18Z, just 5 days after genesis (Cangialosi et al., 2018). Irma's intensity was underforecasted in these beginning stages because of the storm's extended period of RI. Cangialosi et al. (2018) note that Irma's passage over an area of higher sea surface temperatures (SST) played a significant role in the TC's intensity between 2 and 4 September, as the storm steadily intensified and underwent RI thereafter (Figure 1a). Hurricane Irma also passed over the core of the Amazon-Orinoco River plume during RI (~55°W–60°W; Figure 1b), a notable low surface salinity lens that is at a maximum during the peak of Atlantic Hurricane season (Ffield, 2007). During the late summer and fall months, this lens aids in the creation of an oceanic "barrier layer" (Lukas & Lindstrom, 1991; Mignot et al., 2012; Pailler et al., 1999), a subsurface layer where a vertical salinity gradient is present within the uniform temperature mixed layer.

Numerous studies have indicated how deep thermal ocean structure and warm SSTs provide the necessary energy for TC intensification through energetic air-sea fluxes (e.g., Emanuel, 1999; Jaimes & Shay, 2009, 2015; Jaimes et al., 2015; Lin et al., 2005; Shay et al., 2000; Wada & Chan, 2008). A growing amount of studies have investigated the impact of barrier layers and subsurface salinity structure on TC intensification (Androulidakis et al., 2016; Balaguru et al., 2012; Domingues et al., 2015; Ffield, 2007; Hernandez

Resources: Sue Chen, Elizabeth R. Sanabia, Steven R. Jayne
Supervision: Sue Chen
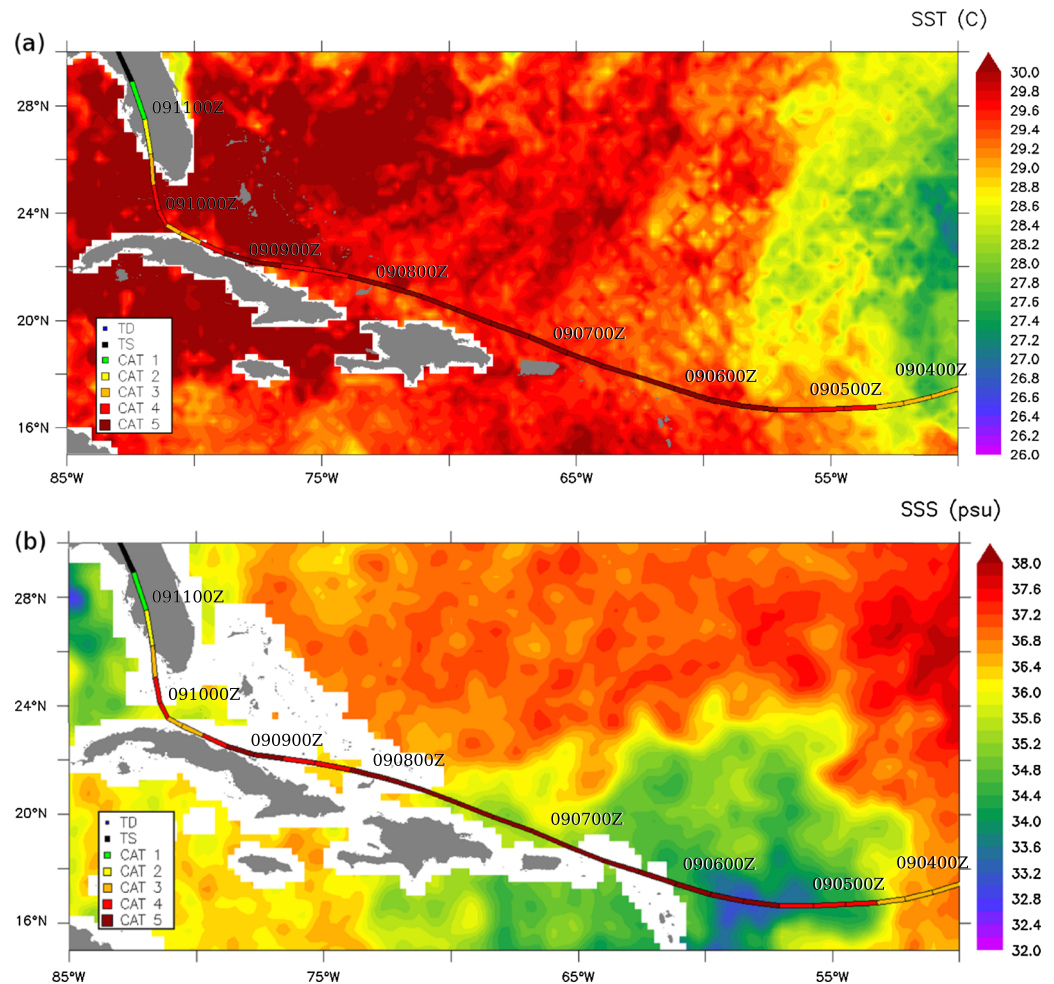**Writing – review & editing:** Sue Chen, Steven R. Jayne

Figure 1. (a) Pre-storm SST and (b) pre-storm SSS with Irma's track overlaid. Storm intensity indicated by color on track. Dates for corresponding track location listed along track in format MMDDHHZ.

et al., 2016; Hlywiak & Nolan, 2019; Newinger & Toumi, 2015; Reul et al., 2014; Rudzin et al., 2018, 2019; Vincent et al., 2014; Vissa et al., 2013; Yan et al., 2017), but most of these studies focus on the ocean response rather than the coupled air-sea response and the mechanisms behind TC intensification. Furthermore, many of these studies use statistical analyses and metrics to correlate ocean parameters to TC intensity rather than investigate dynamic ocean and atmospheric processes that lead to TC intensity change (e.g., Ffield, 2007; Newinger & Toumi, 2015).

Barrier layers are known to suppress turbulent heat flux between the oceanic thermocline and the sea surface because of the strong stability within the layer (Chi et al., 2014; Lukas & Lindstrom, 1991; McPhaden & Foltz, 2013; Mignot et al., 2012). Thus, during strong wind forcing, the SST response is reduced, influencing surface flux into a TC and, theoretically, its intensity. Using a high-resolution regional coupled model, Balaguru et al. (2012) showed that TC intensification rate is nearly 50% higher over regions with barrier layers, compared to regions without. Androulidakis et al. (2016) also used a high-resolution coupled model for three different TCs that passed over the Amazon-Orinoco River plume and found that the presence of a barrier layer during TC passage played a role in the storm's intensification. Hlywiak and Nolan (2019) conducted several idealized, coupled modeling experiments with varying barrier layer structures and TC intensities and concluded that thick barrier layers favor TC intensification because of reduced SST cooling. However, these studies still do not explicitly investigate the link between ocean response, the atmospheric boundary layer, and TC intensity.

Recently, Rudzin et al. (2019) used a suite of in situ atmospheric observations and satellite ocean observations to show how the barrier layer and salinity stratification reduce the efficiency of upper-ocean mixing, reduce SST cooling, and help sustain energetic surface fluxes into a passing TC compared to thermal regimes that do not have this feature. However, the authors (1) did not have in situ oceanic observations to examine upper ocean response and (2) they did not thoroughly investigate how air-sea fluxes influence atmospheric boundary layer thermodynamics, the link between ocean response and TC intensity (Cheng & Wu, 2018; Emanuel, 1986, 1999; Malkus & Riehl, 1960; Murthy & Boos, 2018; Zhang et al., 2017; Zhang & Emanuel, 2016). Malkus and Riehl (1960) first presented that TC intensification was only possible through latent and sensible heat release from the ocean such that pressure decrease is a function of equivalent potential temperature (θ_E) obtained within the TC inflow. More recently, new paradigms are emerging that support the idea that surface fluxes can aid in the recovery of the atmospheric boundary layer via θ_E when environmental vertical wind shear and/or convective downdrafts push low entropy air into the atmospheric boundary layer (Cione et al., 2000; Molinari et al., 2013; Riemer et al., 2010; Rogers et al., 2016; Wadler et al., 2018; Zhang et al., 2013, 2017). The relationship between environmental vertical wind shear direction and the location of eyewall convection has been documented in numerous studies (e.g., Corbosiero & Molinari, 2003; Frank & Ritchie, 2001; Reasor et al., 2000; Riemer et al., 2010; Rogers et al., 2003). Riemer et al. (2010) presented the theory that atmospheric boundary layer air within the eyewall region gets "flushed" with lower entropy (low θ_E) air because of convective downdrafts. These flushing events mainly occur on the upshear sides of the TC and affect intensification. Upshear-left, upshear-right, downshear-left, and downshear-right are terminology used to describe TC quadrants with respect to the direction of vertical wind shear vector. Zhang et al. (2013, 2017) have demonstrated how the recovery of θ_E within the TC inflow layer can be entirely supported by latent and sensible heat in a vertical wind-shear coordinate conceptual model. Zhang et al. (2013) first proposed in this conceptual model that air parcels acquire heat and moisture from air-sea fluxes from the upshear-left to upshear-right quadrants, increasing inner-core θ_E. Convection is then triggered in the downshear-right quadrant, where θ_E becomes a maximum, and cool, dry downdrafts transport low θ_E air to the surface in the downshear-left quadrant. Parcels are then cycled back into the upshear-left quadrant where θ_E increases again as a function of the air-sea fluxes the parcel encounters. Their findings and Zhang et al. (2017) highlight that surface fluxes oppose boundary layer flushing of low entropy air in the upshear quadrants, and help sustain warm, moist boundary layer conditions, favorable for TC intensity change.

Hence, it is of interest to investigate the coupled air-sea response before and during Irma's RI when the TC is interacting with the Amazon-Orinoco River plume, given that previous literature indicates the plausibility of this region providing positive air-sea feedback for intensity change. Prior studies, like Rudzin et al. (2019), show the influence of the Amazon-Orinoco River plume on air-sea fluxes during TCs, but do not relate the ocean state or air-sea fluxes to the atmospheric boundary layer response or TC intensity. Furthermore, the novel oceanic profiling floats utilized in this study, unlike prior studies, provide detailed observations of the upper ocean response (see Sanabia & Jayne, 2020). The key objectives of this work are to identify (1) the influence of salinity stratification on SST cooling utilizing these new oceanic observations and (2) to estimate the atmospheric boundary layer response with respect to the ocean response, air-sea fluxes, and θ_E. Is there any evidence to suggest that the underlying oceanic structure over the Amazon-Orinoco River plume facilitated SST response, air-sea transfer, enhanced boundary layer moist entropy, and facilitated Irma's RI over this region?

2. Data

2.1. In Situ Data

Hurricane Irma was comprehensively sampled in both the atmosphere and the ocean compared to other TCs in this region (Figure 2). Thus, this storm provides a unique opportunity to study the air-sea response during a TC over the Amazon-Orinoco River plume that was previously limited in literature. Periods of interest for this study include 4 September 2017 before Irma's RI and 5 September 2017 during Irma's RI. During these two time periods, a total of 158 dropwindsondes and 22 Aircraft-eXpendable BathyThermographs (AXBT) were deployed in addition to hundreds of subsurface ocean temperature and salinity profiles obtained from Air-Launched Autonomous Micro Observer (ALAMO) floats (Sanabia & Jayne, 2020) (Figure 2).
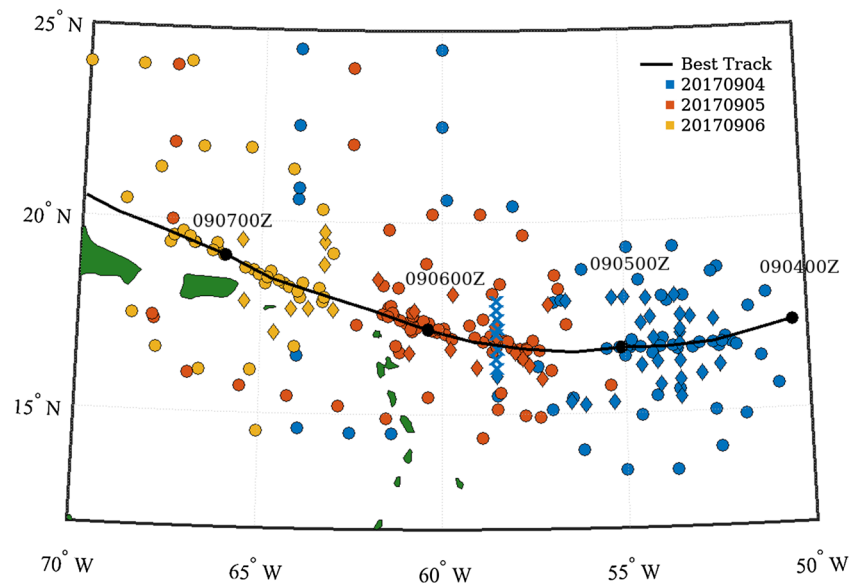
Figure 2. Drop locations of atmospheric dropsondes (circle), AXBTs (diamonds), and ALAMO floats (X's) color coded by time of drop with ATCF best track overlaid for the period of study. Dates for corresponding track location listed along track in format MMDDHHZ. Black circles along track indicate 00Z storm locations. Color of ALAMO floats indicate deployment time only and not all times of subsequent profiles.

Global positioning system dropwindsondes (herein referred to as dropsondes) provide vertical atmospheric profiles of air temperature, wind speed, wind direction, and relative humidity (Hock & Franklin, 1999). Dropsonde data are obtained from NOAA's Hurricane Research Division and are postprocessed using National Center for Atmospheric Research (NCAR) ASPEN (Atmospheric Software Processing Environment) software, which quality controls each dropsonde sounding.

AXBTs are aircraft deployable oceanographic instruments that measure subsurface ocean temperature (Sanabia et al., 2013). Profiles are returned to aircraft via radio and are later interpolated to 1-m vertical resolution. Temperature measurements are accurate to 0.2°C (Dinegar Boyd, 1987).

ALAMO floats are oceanic profiling floats, developed by MRV Systems, that measure subsurface ocean temperature and salinity while descending/ascending the ocean column via a buoyancy driven engine (Jayne & Bogue, 2017). The floats are air-deployable from C-130 aircraft. ALAMO floats are capable of 100–150 profiles up to 1,000-m depth and have an initial temperature accuracy of 0.002°C and an initial conductivity accuracy of 0.003 S m^{-1}.

2.2. Satellite Data

To supplement in situ data described above, satellite SST and sea surface salinity (SSS) are obtained to distinguish the mesoscale ocean response along Irma's track. Daily satellite SSTs are obtained from the Jet Propulsion Laboratory's PODAAC Group for High Resolution Sea Surface Temperatures (GHRSST) Level 4 MUR (JPL MUR MEaSUREs Project, 2010). This product provides daily 1-km blended Level 4 global SST analyses and is chosen for its high resolution to resolve oceanic fronts and that it incorporates microwave sensors, which are needed to resolve SST variability in cloudy environments. The accuracy of resolving SSTs in TC environments using this product can be found in Rudzin et al. (2019). Satellite SSS is obtained from the CATDS (Centre Aval de Traitement des Données SMOS) 9-day 25-km Level 3 debiased SSS product from the European Space Agency's Soil Moisture and Ocean Salinity (SMOS) mission (Boutin et al., 2018).

Pre-storm and post-storm dates are chosen with respect to each product's temporal availability and such that a full ocean response can be acquired for the entire Caribbean Sea and surrounding areas. Satellite SSS observations have a 9-day temporal resolution (satellite swaths averaged over 9 days) with the date of interest centered between the ± 4 days. Pre-storm satellite observations for SST (SSTpre) are obtained from 3 September 2017 whereas pre-storm observations for SSS (SSSpre) are obtained from 31 August 2017. The temporal

Table 1
Estimates of Air-Sea Parameters per 6 hr per Time Period

	Time 1 (pre-RI)				Time 2 (RI)			
	00Z	06Z	12Z	18Z	00Z	06Z	12Z	18Z
V_{max} (m s^{-1})	51.4	51.4	54.0	59.1	61.7	69.4	79.7	82.2
R_{max} (km)		27.8				27.8		
U_h (m s^{-1})	6.2	6.5	4.6	6.4	5.9	6.4	6.9	7.0
IP (hr)		41.0				34.8		
λ^x (km)	922	972	673	950	884	961	1,034	1,042
L_η (km)		111.2				111.2		
τ (hr)	5.0	4.7	6.8	4.8	5.2	4.8	4.5	4.4

Note. Definitions of parameters are in section 3.

resolution of these data choices limit the mesoscale pre-storm and post-storm environment assessment bias. SSSpre data cannot be obtained on the same day at SSTpre data because of the temporal resolution of the SSS data. Poststorm SST and SSS (SSTpost and SSSpost, respectively) are obtained from 12 September 2017 for both SST and SSS. Change in SST (ΔSST) and change in SSS (ΔSSS) are estimated as ΔSST = SSTpost − SSTpre and ΔSSS = SSSpost − SSSpre.

3. Methods

This study will focus on two particular time periods as Hurricane Irma undergoes RI over the Amazon-Orinoco River plume region: (1) the time period prior to RI (referred to as "pre-RI") and (2) the time period during RI (referred to as "RI"), respectively. We utilize the definition of RI from the National Hurricane Center as an increase in maximum sustained wind speed of at least 30 kt (15.4 m s^{-1}) over a 24-hr period. Maximum wind speed (V_{max}) increases by 10.3 m s^{-1} from 4 September 00Z to 5 September 00Z, whereas V_{max} increases by 20.5 m s^{-1} from 5 September 00Z to 18Z, indicating RI over 5 September and the time before RI (pre-RI) over 4 September. All in situ data collected on 4 September 2017 will be grouped into the pre-RI time period and all in situ data collected on 5 September 2017 will be grouped into the RI time period for the sake of this study, denoted in Table 1 for 4 September 2017 and 5 September 2017. "Pre-storm" and "in-storm" refers to the time periods in which the data was collected before storm passage and during storm passage, respectively, in the areas that pre-RI and RI took place. For example, Hurricane Irma's eye passed over deployed ALAMO oceanic profiling floats (section 4.2) approximately 5 September 16Z. Therefore, the time period before this is considered "pre-storm."

3.1. Definition of Ocean Variables

Several different air-sea parameters are summarized in Table 1 to get a broad overview of TC size, intensity, and translation speed as well as the storm's projected influence on the ocean in the pre-RI and RI regions. Radius of maximum winds (R_{max}) and maximum wind speed (V_{max}) are obtained from the Automated Tropical Cyclone Forecast (ATCF) 6-hourly best track data set (Sampson & Schrader, 2000) to measure storm size and intensity at the two time periods of interest. Irma's translation speed (U_h) is inferred from best track data. Ocean inertial period (IP), along-track predicted wavelengths ($\lambda^x \approx U_h * IP$; Price, 1983), cross-track width of the sea-surface height response in the wake ($L_\eta \approx 4 * R_{max}$; Price, 1983), and the time available for turbulent mixing ($\tau = 4 * R_{max} * U_h^{-1}$; Greatbatch, 1983) are estimated to identify the ocean response in relation to storm size and speed.

Other variables that are estimated from both AXBT and ALAMO profiles are the oceanic mixed layer depth (MLD), the oceanic isothermal layer depth (ILD), Brunt-Väisälä frequency (N), barrier layer thickness (BLT), and oceanic heat content relative to the 26°C isotherm (OHC, Leipper & Volgenau, 1972) (Table 2). MLD is defined where both properties of temperature and salinity are constant with depth such that potential density (σ_θ) has increased from a reference depth (i.e., surface) by a threshold of $\Delta\sigma = \sigma_\theta(T_0 - 0.5, S_0, P_0) - \sigma_\theta(T_0, S_0, P_0)$ (de Boyer Montégut et al., 2007), where T_0, S_0, and P_0 are surface values of ocean temperature, salinity, and pressure, respectively. ILD is defined where ocean temperature is constant with depth and is estimated as ILD = SST − 0.5°C. Barrier layer thickness is computed to identify if the background salinity stratification induced by the river plume creates a barrier layer (Sprintall & Tomczak, 1992). BLT is the layer thickness between the ILD and MLD (BLT = ILD − MLD). Brunt-Väisälä frequency is estimated using ocean temperature and salinity, and profiles of N are smoothed using a running mean filter to remove excess noise. The maximum value of Brunt-Väisälä frequency is denoted as N_{max}.

3.2. Definition of Atmospheric Variables

Temperature, relativity humidity, and wind speed and direction are used from each shear-relative profile to compute specific humidity (q), potential temperature (θ), equivalent potential temperature (θ_E, Equation 1; Bolton, 1980), tangential wind speed (V_t), and radial wind speed (V_r). In Equation 1, T_{LCL} is the temperature

Table 2

Mean ± 1 Standard Deviation of Ocean Variables as Measurement by AXBTs and ALAMO Floats Separated by Pre-RI and RI Area

	Pre-RI pre-storm 09-04 00Z AXBT	Pre-RI in-storm 09-04 16Z to 09-05 00Z AXBT	RI pre-storm 09-05 08–10Z ALAMO	RI in-storm 09-05 15–19Z ALAMO	RI in-storm 09-05 15–18Z AXBT
SST (°C)	28.7 ± 0.4	28.5 ± 0.5	29.2 ± 0.2	29.1 ± 0.1	28.6 ± 0.4
SSS (psu)			33.9 ± 0.7	34.1 ± 0.8	
MLD (m)			18.7 ± 6.9	17.4 ± 9.1	
ILD (m)	42.7 ± 13.2	44.8 ± 12.4	35.3 ± 5.8	37.6 ± 5.9	44.4 ± 8.7
OHC (kJ cm^{-2})	64.2 ± 14.5	59.7 ± 14.0	68.6 ± 4.4	67.9 ± 4.6	66.3 ± 13.9
BLT (m)			16.6 ± 9.1	20.2 ± 8.7	
N_{max} (cph)			29.7 ± 4.7	29.2 ± 6.1	

Note. Variables derived using salinity are left blank for AXBT columns since these instruments do not measure salinity. Times listed in heading indicate the collection time of the group of observations.

at the lifting condensation level, L_v is the latent heat of vaporization, and C_p is specific heat of air at constant pressure.

$$\theta_E = \theta exp\left(\frac{L_v q}{C_p T_{LCL}}\right). \tag{1}$$

Ten-meter values of temperature, q, and θ_E are extracted from each profile to compare lower-level atmospheric environments between the two time periods and are used to assess the influence of surface fluxes on boundary layer θ_E recovery (further discussed in section 4.3). In this context, the "atmospheric boundary layer" is the vertical region over which the TC inflow occurs, which is the estimated kinematic boundary layer height where tangential wind speed is maximum (as in Zhang et al., 2011, obtained from dropsondes for each time period). The boundary layer recovery analysis is performed to identify the impact of the ocean response and SST cooling on surface fluxes and how this directly modulates atmospheric boundary layer thermodynamics. Tangential and radial winds are computed by removing the storm-relative motion from u and v wind components and transforming u and v wind components to tangential and radial wind components relative to the storm center for each dropsonde. The storm center for each dropsonde is the location of the storm at the time of each dropsonde deployment. Tangential wind speed is primarily computed to estimate the top of the inflow layer as described in Zhang et al. (2013) and to use in the trajectory time estimate in section 4.3.

Latent and sensible heat fluxes are estimated for dropsondes that have a corresponding AXBT SST measurement (Table 3). Total enthalpy (Q_h), latent (Q_l), and sensible (Q_s) heat flux are estimated by

$$Q_l = \rho L_v C_q U_{10}(q_{SST} - q_{10}), \tag{2}$$

$$Q_s = \rho C_p C_h U_{10}(SST - T_{10}), \tag{3}$$

$$Q_h = Q_l + Q_s, \tag{4}$$

where q_{SST} is the saturation specific humidity at SST (assumed to be at 98% saturation at the SST; Buck, 1981), q_{10} is the specific humidity of the air at 10 m, U_{10} is wind speed at 10 m, $\rho = 1.22$ kg m^{-3}, $L_v = 2.5 \times 10^6$ J kg^{-1}, and $C_p = 1{,}004.7$ J K^{-1} kg^{-1}. C_h and C_q are assumed to be equal such that $C_h = C_q = C_k$ where enthalpy exchange coefficient C_k is determined from Haus et al. (2010). Given that Irma's wind speeds are greater than 50 m s^{-1} for pre-RI and RI, $C_k = 1.0 \times 10^{-3}$. Because there are very limited double drops of AXBTs and dropsondes together, SST for latent and sensible heat flux estimation for the atmospheric boundary layer recovery analysis will be approximated from an SST objective analysis (OA) field created from in-storm AXBTs (Figure 3).
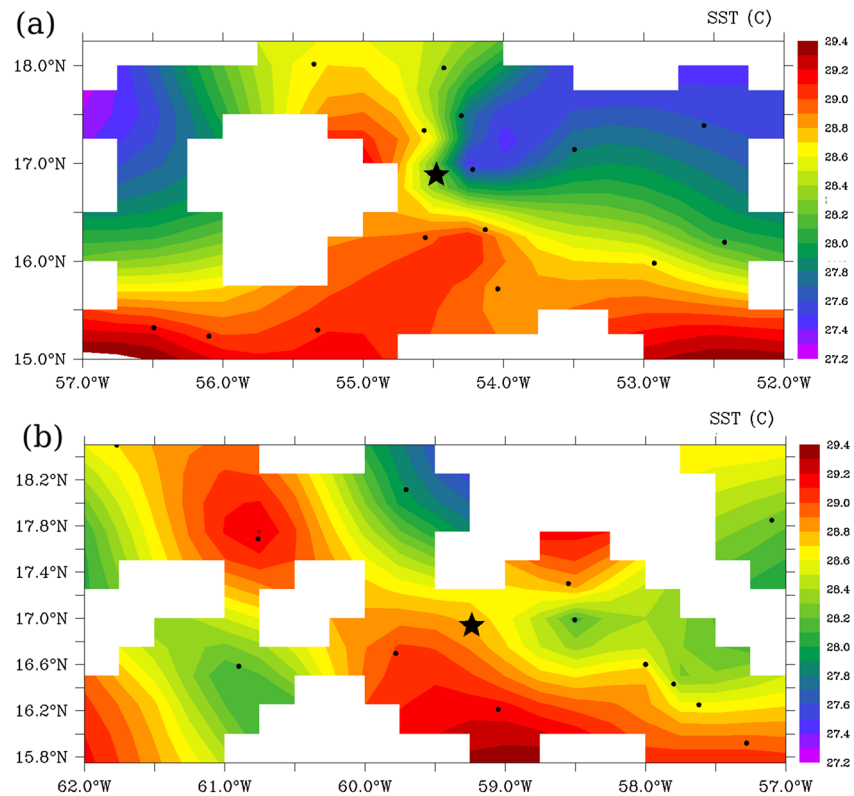
Table 3

Air-Sea Fluxes Estimated From AXBT/Dropsonde Double Drops That are Within 0.25° of Each Other

Sonde drop time	AXBT drop time	Latent heat flux (W m^{-2})	Sensible heat flux (W m^{-2})
2017090416	2017090400	454.2	132.3
2017090410	2017090401	248.0	16.2
2017090409	2017090500	205.9	10.2
2017090511	*2017090513*	*1,157.1*	*299.9*
2017090602	*2017090523*	*1,642.7*	*387.6*

Note. Values denoted in italics are within the TC inner core (≤ 1 R_{max}) and instrument drops are within 6 hr of each other. These sonde are denoted in Figure 7 as blue (2017090511 drop) and magenta (2017090602 drop) circles.

Figure 3. Objectively analyzed SST from in-storm AXBT deployments for (a) pre-RI time period and (b) RI time period. Black circles indicate AXBT locations. Black stars indicate the approximate location of Irma during the AXBT flights. White areas are regions where there are no observations within 0.5° of the nearest observations. In-storm AXBT flights consist of those on 4 September 1730Z and 2330Z for pre-RI and 5 September 1130Z and 2330Z for RI.

3.3. TC-Relative and Shear-Relative Coordinates

Dropsonde observations that are collected for the two time periods are grouped together such that all of them occur on the same day: observations from 4 September 2017 for pre-RI and 5 September 2017 for RI. Observations are referenced from a Cartesian coordinate system to a TC-relative coordinate system with respect to the TC center and then into "shear-relative" coordinate system with respect to the deep-layer vertical environmental wind shear vector. Deep-layer vertical environmental wind shear (850–200 hPa) direction is obtained at 6-hr time intervals from the Statistical Hurricane Intensity Prediction Scheme (SHIPS) data set (DeMaria et al., 2005). The shear direction for an observation is based on the 6-hr time interval that observation is nearest to. The average deep-layer vertical environmental wind shear for 4 and 5 September is northerly (181°) and northwesterly (165°) shear, respectively, based on the definition of SHIPS deep shear vector (90° = westerly shear). The storm center for each dropsonde observation is obtained from ATCF best track and based upon the time that observation was collected. The latitudinal and longitudinal coordinates for the dropsonde locations are converted into a radius length away from the storm center normalized by the R_{max} based on the time the data point was collected. Then, these points are referenced into a shear-relative coordinate system by rotating the original Cartesian axes such that the x-axis separates the upshear and downshear quadrants and the y-axis separates the left and right of the deep vertical wind shear vector. The positive y direction is the direction of deep vertical wind shear vector. An observation is designated within the upshear-left (USL), upshear-right (USR), downshear-right (DSR), or downshear-left (DSL), depending on each sonde's location relative to the TC center and the deep-layer wind shear vector at the time of observation. The data are referenced using a shear-coordinate system because numerous studies have utilized this coordinate system to understand how TC boundary layer thermodynamics are modulated by environmental wind shear (Cione et al., 2000; Molinari et al., 2013; Powell, 1990; Sitkowski & Barnes, 2009; Wadler et al., 2018; Zhang et al., 2013, 2017). While the goal of this work is to identify links between

ocean response and the modulation of inner-core TC atmospheric boundary layer thermodynamics rather than influences of shear on convection, using this reference system provides context from previous work to interpret results from our boundary layer thermodynamic analyses.

3.4. Estimation of Dynamic Potential Intensity

To further demonstrate the influence of salinity stratification on TC intensity, dynamical potential intensity (DPI; Balaguru et al., 2015) is estimated and compared to the original formulation of potential intensity (PI; Emanuel, 1999). The differences between PI and DPI between the pre-RI and RI periods are also assessed to examine if these metrics capture Irma's RI and, thus, justify the ocean's role in facilitating intensity during RI.

Potential intensity is the theoretical limit to the maximum intensity that can be sustained by a TC and uses SST to approximate ocean influence. The formulation for PI is

$$PI = V_{max}^2 = \frac{SST - T_0}{T_0} \frac{C_K}{C_D} (k_{SST} - k),$$

(5)

where T_0 is hurricane outflow temperature, C_K is the enthalpy exchange coefficient, C_D is the momentum drag coefficient, $k_{SST} = L_v q_{SST} + C_p SST$ is the enthalpy of air in contact with the sea surface, and $k = L_v q_{10a} + C_p T_{10a}$ is the specific enthalpy of air near the surface. The ratio of enthalpy exchange and momentum drag coefficients are set to equal 1. In contrast, DPI estimates TC potential intensity using a depth-integrated temperature (T_{dy}; instead of SST) that includes the influence of ocean density stratification through a mixing length, L_{pred},

$$L_{pred} = h + \left(\frac{2\rho_0 u_*^3 t}{\kappa g \alpha} \right)^{\frac{1}{3}},$$

(6)

$$T_{dy} = \frac{1}{L} \int_0^L T(z) dz,$$

(7)

where h is pre-storm MLD, ρ_0 is seawater density, u_* is surface friction velocity, t is the time period of mixing ($t = R_{max}/U_h$), κ is the von Karman constant equal to 0.4, and α is the pre-storm vertical potential density gradient beneath the mixed layer (the stratification term). Pre-storm MLD is used for h instead of in-storm values since L_{pred} is used to forecast a mixing length; the density stratification term, α, is also estimated using pre-storm profiles. SST for PI estimates is obtained from in-storm ocean observations, and q_{SST} is the saturation specific humidity at SST (assumed to be at 98% saturation at the SST; Buck, 1981). In both PI and DPI estimates, T_{10a} and q_{10a} are the average 10-m air temperature and specific humidity, respectively, estimated from all of the dropsondes for the day of interest (either pre-RI or RI). Outflow temperature ~218 K (for both pre-RI and RI) is obtained from the ERA-interim data set (Dee et al., 2011) and estimated by averaging air temperature between 100–300 hPa over the TC center for the time period of interest.

Two of the main sensitivities in the DPI formulation are momentum flux and stratification. Tables 4 and 5 show the sensitivities of u_*, L_{pred}, respective T_{dy}, and TC DPI for the pre-RI and RI period, respectively, to different values of momentum drag coefficient for high wind speeds reported in literature and two stratification strengths. A further explanation of these tables is in section 4.3.3.

4. Results

4.1. Synoptic Overview of Hurricane Irma Over the Tropical Atlantic

Hurricane Irma originated on 27 August 2018 as a tropical wave off of Cape Verde and rapidly strengthened into a hurricane (70 kt over 48 hr) by 31 August 06Z in low environmental wind shear and increasingly warm ocean waters (Cangialosi et al., 2018). Over the next few days, Irma's intensity remained steady around 100 kt as the major hurricane tracked southwestward in response to strong high pressure system, putting it in line with the Leeward Islands. Irma underwent RI again on 5 September as it closed in on the island chain, intensifying to a Category 5 hurricane. The TC made its first landfall on the island of Barbuda early on 6 September with maximum winds of 155 kt, causing the island to become uninhabitable in the storms' aftermath (Cangialosi et al., 2018).

Table 4

For the Pre-RI Period, Values of Surface Friction Velocity (u_*), Predicted Mixing Length (L_{pred}) From Equation 5, and Depth-Integrated Temperature for L_{pred} (T_{dy}, Equation 6), Which are Used to Estimate Dynamic Potential Intensity (DPI) and Vary Based on Prescribed Momentum Drag Coefficient (C_D) for Observed Stratification (Full α) and Half of Observed Stratification (Half α)

	C_D (×10^{-3})	u_*	L_{pred} (m) full α	T_{dy} (°C) from L_{pred} full α	DPI (m/s) full α	L_{pred} (m) half α	T_{dy} (°C) from L_{pred} half α	DPI (m/s) half α	In-storm SST (°C)	PI from in-storm SST (m/s)	V_{max} (m/s)
Powell et al., 2003	2.6	0.103	64.8	27.9	42.6	76.5	27.6	37.5	28.5	56.2	59.1
Donelan et al., 2004	2.3	0.097	62.2	27.9	46.7	73.1	27.7	41.3	28.5	56.2	59.1
Jarosz et al., 2007	1.7	0.083	56.2	28.1	49.7	65.7	27.9	44.8	28.5	56.2	59.1
Soloviev & Lukas, 2010	1.1	0.067	49.2	28.3	52.8	56.7	28.1	49.2	28.5	56.2	59.1
Bell et al., 2012	1.4	0.076	52.9	28.2	51.1	61.4	28.0	47.3	28.5	56.2	59.1
Donelan, 2018	1.4	0.076	52.9	28.2	51.1	61.4	28.0	47.3	28.5	56.2	59.1

Note. TC potential intensity (PI), based on in-storm SST, and V_{max} (from Table 1) are provided for context. α, L_{pred}, and T_{dy} are estimated from the AXBT pre-storm temperature profile (Figure 5) and a climatological salinity profile from World Ocean Atlas 2013 for the closest 0.25° location. In-storm SST is from the AXBT in-storm profile (Figure 5).

4.2. Ocean Response

Figure 4 shows the basin-scale ocean temperature and salinity response as a result of Irma's passage. Overall, the largest SST and SSS response occurs on the right side of the storm, consistent with previous literature (Price, 1981). Both maximums (ΔSST ~3°C cooling, ΔSSS ~2.6 psu increase in salinity) occur where Irma underwent RI over the river plume area between 55°W and 60°W within Irma's 34 kt wind maximum (Figure 4). This suggests a strong upwelling of cool, salty subsurface waters. Another large area of SST cooling to note is over the Bahama Banks that is most likely caused by intense mixing over very shallow waters in the area.

However, various air-sea parameters estimated in Table 1 suggest that this enhanced SST cooling and increase in salinity in the RI region may not have all occurred during the time Irma passed over this area. Comparing the time available for turbulent mixing (τ ~ 4.4 to 5.2 hr) to the long IP (34.8 hr) in this region reveals that a large contribution of the cooling depicted in Figure 4 is likely to be a result of the near-inertial wave wake that occurs behind a TC (Geisler, 1970; Jaimes & Shay, 2010; Shay et al., 1989). The details about the near-inertial wake are further explained in Sanabia and Jayne (2020).

We are able to investigate the forced-stage component (when the TC is interacting with the area of interest) of the ocean response for these two time periods given the array of pre-storm and in-storm AXBTs deployed for the pre-RI area, in-storm AXBTs for the RI area, and pre-storm, during, and poststorm profiles observed via ALAMO floats for the RI area (Figure 2; see Sanabia & Jayne, 2020). Mean and standard deviation values for each time period are presented in Table 2 and are denoted whether the observations were taken before, during, or after storm passage and whether they are retrieved by AXBT or ALAMO. Observed pre-storm SSTs are approximately the same between the pre-RI and RI region (Table 2) even though satellite observations in Figure 1 show a horizontal SST gradient between the two areas. Moreover, their average thermal structure is

Table 5

Same as Table 4 but for the RI Period

	C_D (×10^{-3})	u_*	L_{pred} (m) full α	T_{dy} (°C) from L_{pred} full α	DPI (m/s) full α	L_{pred} (m) half α	T_{dy} (°C) from L_{pred} half α	DPI (m/s) half α	In-storm SST (°C)	PI from in-storm SST (m/s)	V_{max} (m/s)
Powell et al., 2003	2.6	0.144	62.1	28.5	68.3	73.8	28.2	63.9	29.1	76.1	82.2
Donelan et al., 2004	2.3	0.135	59.4	28.6	69.6	70.4	28.3	65.2	29.1	76.1	82.2
Jarosz et al., 2007	1.7	0.116	53.5	28.8	72.3	62.9	28.5	67.9	29.1	76.1	82.2
Soloviev & Lukas, 2010	1.1	0.093	46.3	29.0	74.7	54.0	28.8	71.9	29.1	76.1	82.2
Bell et al., 2012	1.4	0.105	50.1	28.9	73.4	58.7	28.6	69.6	29.1	76.1	82.2
Donelan, 2018	1.4	0.105	50.1	28.9	73.4	58.7	28.6	69.6	29.1	76.1	82.2

Note. In-storm SST, α, L_{pred}, and T_{dy} are estimated from ALAMO float 9134, with in-storm SST being extracted during TC passage (15Z) and the latter three variables are estimated from profiles before storm passage (5 September 9Z).
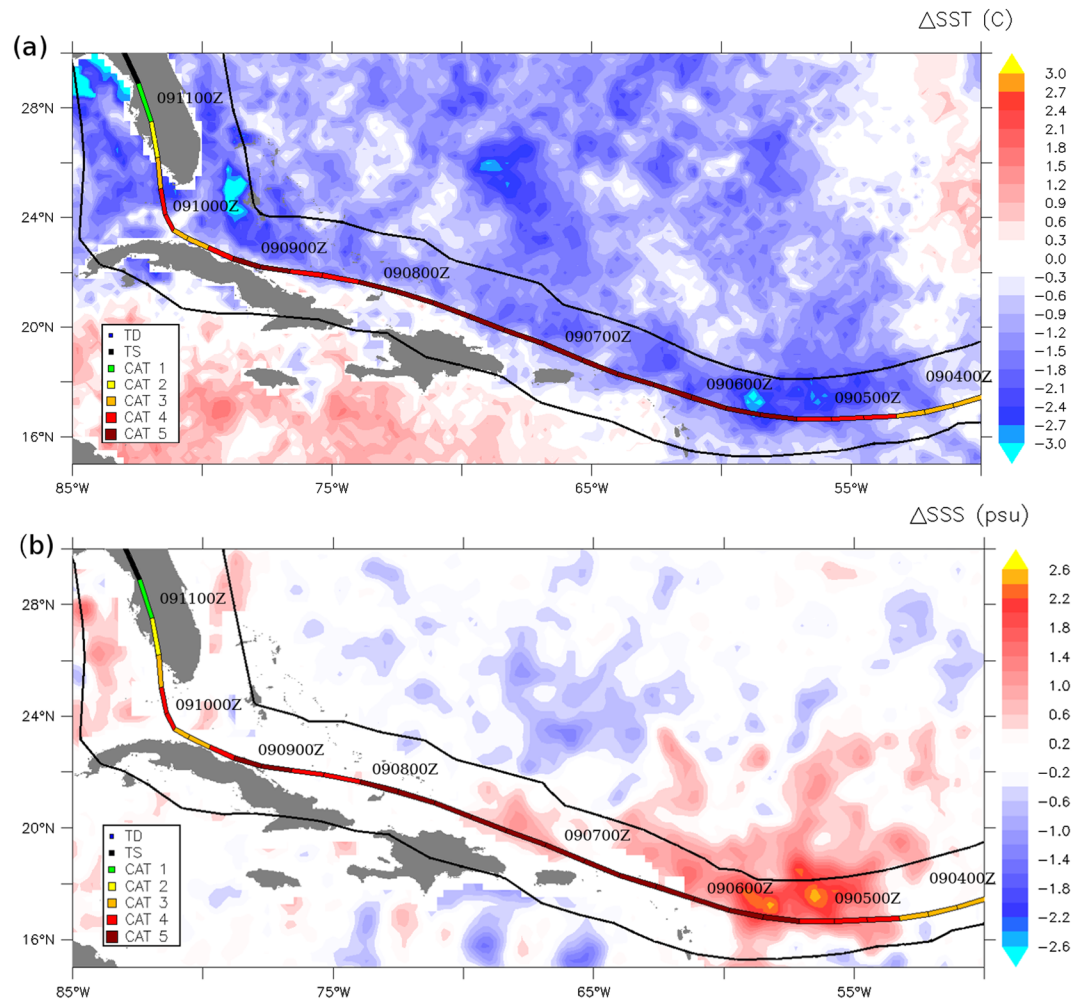
Figure 4. (a) ΔSST and (b) ΔSSS with Irma's track overlain. Black lines indicate extent of 34 knot wind field. Storm intensity indicated by color on track.

fairly similar with regards to ILD and OHC. Salinity observations collected via ALAMO also indicate the presence of a pre-storm barrier layer (mean BLT ~ 16.6 m) and a strongly stratified upper ocean. Mean pre-storm N_{max} within the barrier layer is upwards of 30 cph, which is very high in comparison to prior studies documenting Brunt-Väisälä frequency induced by river outflow in this area (Rudzin et al., 2017).

A mean surface salinity increase of ~0.2 psu (up to ~1 psu including variability among floats) is observed during TC passage throughout the ALAMO floats, indicating some upwelling in the RI region. SST response differences are hard to identify looking at the average difference between pre-storm and in-storm SST between the two regions. Mean ΔSST is approximately 0.2°C for the pre-RI region from 0Z to 18Z on 4 September and mean ΔSST for the RI region is 0.1°C from 5 September 09Z to 5 September 19Z. However, analyzing the changes between individual profiles clearly shows that the subsurface and surface responses differ between the pre-RI and RI regions.

Figure 5 shows the pre-storm and in-storm temperature profiles from two different AXBTs: the pre-storm AXBT is deployed 18 hr prior to Irma's passage (4 September 00Z) and the in-storm AXBT is deployed during Irma's passage (4 September 18Z). They were dropped approximately 10 km apart in the pre-RI region. The in-storm AXBT temperature profile was observed 65.5 km northeast of the storm center, approximately 2.5 R_{max}. The change in SST from storm forcing is approximately 1°C, the ILD deepens to 41 m from 28 m, and OHC decreases from 53.1 to 45.8 kJ cm^{-2} (53.1 to 45.8 × 10^7 J m^{-2}) (Figure 5). This SST cooling can also be
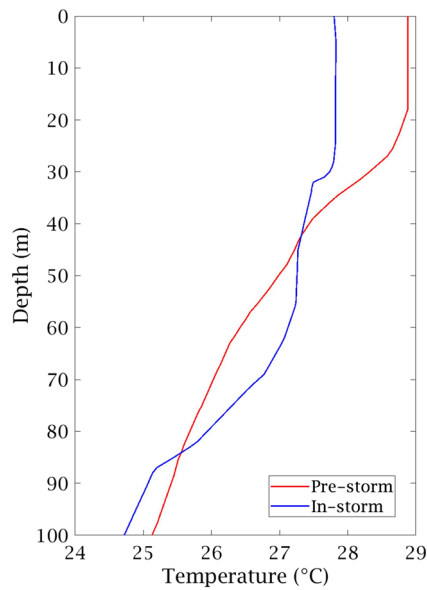
Figure 5. Temperature profiles from AXBTs observed on 4 September 00Z (red) before Irma passed over the area (pre-storm) and on 4 September 18Z (blue) during Irma (in-storm). Locations for the pre-storm and in-storm profiles are 17.05°N, 53.50°W and 17.14°N, 53.49°W, respectively.

observed in the AXBT OA field, which shows a sharp horizontal SST gradient ahead and behind the TC (Figure 3a).

In contrast, Figure 6 shows the upper ocean temperature, salinity, and Brunt-Väisälä frequency profiles from an individual ALAMO float before, during, and after Hurricane Irma's passage where the TC underwent RI. The pre-storm SST, SSS, MLD, ILD, and OHC for this float on 5 September 09Z are 29.3°C, 33.8 psu, 20 m, 28 m, and 70 kJcm^{-2} (70×10^7 J m^{-2}), respectively. Initial SST is warmer and OHC is higher in this float compared to initial values from the AXBT in Figure 5 by 0.5°C and approximately 17 kJ cm^{-2} (17×10^7 J m^{-2}), respectively, but the ILD is shallower by 13 m. Initial profiles from this float also indicate a preexisting barrier layer of 18 m which is also strongly stratified ($N_{max} \sim 30$ cph) as in the other floats (Table 2). The Amazon-Orinoco River plume most likely contributes to the barrier layer and strong salinity stratification observed, given the floats were deployed in the core of the plume (Figures 1b and 2). TC precipitation has been also shown in literature to also induce fresh water lens and vertical salinity gradients in the upper ocean (Jacob & Koblinsky, 2007; Steffen & Bourassa, 2018). Using satellite SSS weeks before Irma's passage together with pre-storm ARGO float data (Argo, 2000), IMERG precipitation data (Huffman et al., 2014) and one-dimensional ocean mixed layer model simulations (Price et al., 1986) (see the Supporting Information), supporting analyses verify that the preexisting vertical salinity gradient observed is most likely from the Amazon-Orinoco River plume rather than Irma's precipitation.

As the TC passes over the ALAMO float around 5 September 16Z, there is only slight SST cooling of 0.2°C by 5 September 17Z and 0.4°C by 5 September 22Z from the pre-storm SST at 09Z, 1 and 6 hr after storm passage, respectively (Figure 6a). This response is the same order as the rest of the ALAMO floats SST response (~0.4°C ± 0.3°C by 6 September 0Z). This slight cooling can be attributed to the strongly stratified barrier layer remaining fairly unscathed (Figure 6b, 09Z–15Z). Cooling during Irma's passage over the river plume region is less than half of that observed outside the river plume from the AXBTs (Figure 5).

Three hours after eyewall passage (19Z), the vertical maximum in N starts to rapidly decrease with time, indicating vertical mixing is acting to reduce the stratification (Figure 6c). This is accompanied by increasing SSS and decreasing SST. Several hours after Irma's passage (12 hr+), the SST starts to dramatically cool while SSS also rapidly increases (gray lines in Figures 6a and 6b). The magnitudes of these SST and SST responses compare well with the satellite estimates of SST cooling and SSS increase (Figure 4). Sanabia and Jayne (2020) clearly show that the majority of this cooling in Irma's wake is dominated by near-inertial oscillations (Geisler, 1970; Jaimes & Shay, 2010; Shay et al., 1989).

4.3. Atmospheric Boundary Layer Thermodynamics and Air-Sea Interaction
4.3.1. Atmospheric Thermodynamic Variables

Values of T_{10}, q_{10}, and θ_E estimated from dropsondes within 3 R_{max} for the pre-RI and RI time period (Figure 7) are compared to identify thermodynamic differences that exist between the two time periods and if these differences may be linked back to the oceanic response. Note that the dropsondes are collected over multiple flights over the course of 1 day (4 September for pre-RI and 5 September for RI). However, grouping the dropsondes per shear-relative quadrant allows for comparison of thermodynamic properties in each quadrant between these two events, even with lower temporal coverage.

Overall, the spatial pattern of all three variables within the inner-core (~1 R_{max}) is fairly consistent between pre-RI and RI. Maximum values of T_{10}, q_{10}, and θ_{E10} (and their locations) are 28.0°C (downshear right, DSR), 22.9 g kg^{-1} (downshear left, DSL), and 375.5 K (DSL), respectively, for pre-RI and 27.8°C (upshear left, USL), 23.5 g kg^{-1} (DSR), and 379.8 K (DSR) for RI (Figure 7). Equivalent potential temperature decreases radially outwards, is greater than 370 K for both time periods inside 1 R_{max}, and is at a
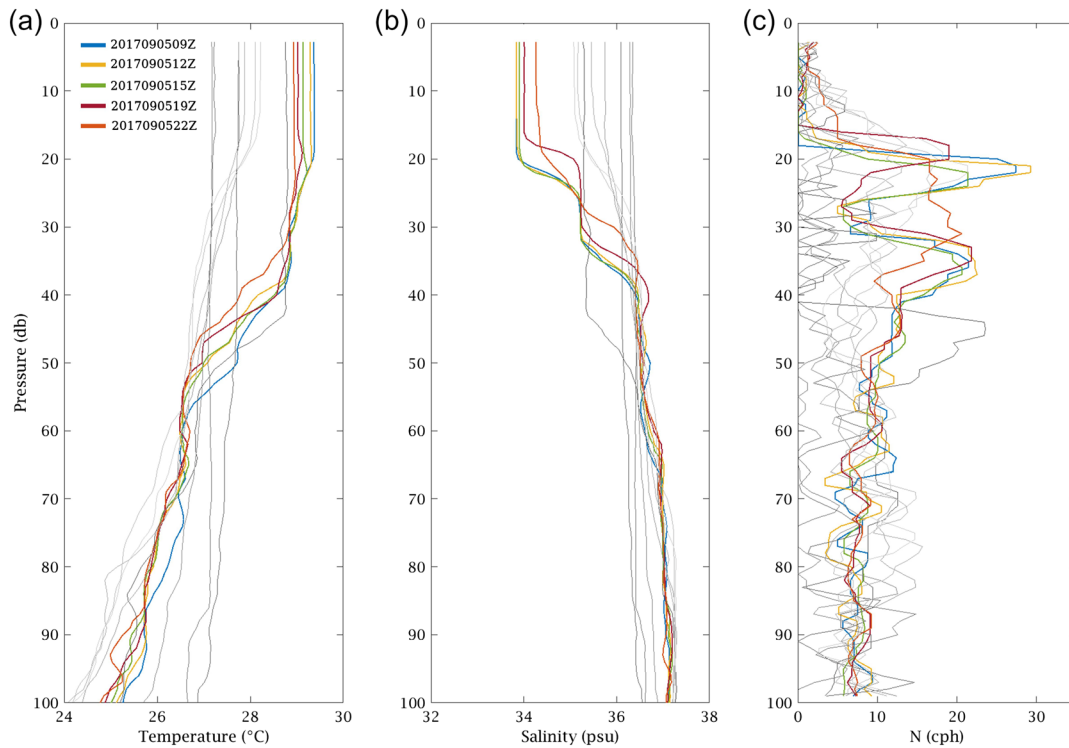
Figure 6. (a) Ocean temperature (in celsius), (b) salinity (in psu), and (c) Brunt-Väisälä frequency (in cycles per hour, cph) of the upper 100 m from ALAMO float 9134. Irma's center passed over ALAMO 9134 at approximately 5 September 16Z. Color profiles indicate times prior and just after Irma's passage. Gray profiles indicate times after approximately 12+ hr after passage.

maximum in the downshear quadrants, which agrees with previous literature in both composite (Zhang et al., 2013) and case study analyses (Schneider & Barnes, 2005; Sitkowski & Barnes, 2009; Zhang et al., 2017). Previous literature has documented the DSR quadrant being an area where deep convection is initiated (Zhang et al., 2013, 2017). Maximum θ_{E10} in the DSR quadrant for RI is 379.8 K, whereas it is 372.7 K for pre-RI (Figure 7), approximately 6 K larger in RI than pre-RI, indicating a much warmer, moist area where deep convection is initiated for the RI time period. Overall, mean θ_{E10} is warmer for each quadrant during RI compared to pre-RI, and this change is mainly controlled by moisture rather than temperature (Figure 7).

Several instances of cool, dry boundary layer air are prevalent during RI compared to pre-RI. Cool ($T_{10} < 20°C$), dry ($q_{10} < 16$ g kg^{-1}) air appears left of the shear vector at 1 R_{max} during the RI period that creates low θ_{E10} air ($\theta_{E10} \sim 352$ K DSL, $\theta_{E10} \sim 355$ K USL) (Figure 7). Data from airborne Doppler radar (not shown) during these flights that dropsonde data is acquired indicate that these areas are collocated with moderately intense rain bands (up to 32 dBZ). The location of these low θ_{E10} areas are similar to past work that has shown the lowest θ_E occurring in the DSL and USL quadrants from convective or mesoscale downdrafts bringing low θ_E into the boundary layer (Molinari et al., 2013; Powell, 1990; Wadler et al., 2018; Zhang et al., 2013, 2017). Wadler et al. (2018) notes that low θ_{E10} that corresponds with weaker downdrafts require relatively more surface fluxes to recover the boundary layer. A warm (~25.4°C), but relatively dry (~20.5 g kg^{-1}) feature within 1 R_{max} is also observed in the DSR quadrant during the pre-RI. These types of features have also been shown to be detrimental to inner-core thermodynamics (Wadler et al., 2018).

Even with these suspected cool, dry downdrafts occurring during the RI period, Irma still undergoes a 40 knot intensification over 5 September. Molinari et al. (2013), Zhang et al. (2017), and Wadler et al. (2018) state that very cool, dry downdrafts, similar to the features seen in the DSL quadrant during RI (Figures 7(1b)–7(3b)), can be a great hindrance for intensification without sufficient surface fluxes. However, the atmospheric boundary layer can recover through air-sea fluxes and a combination of other
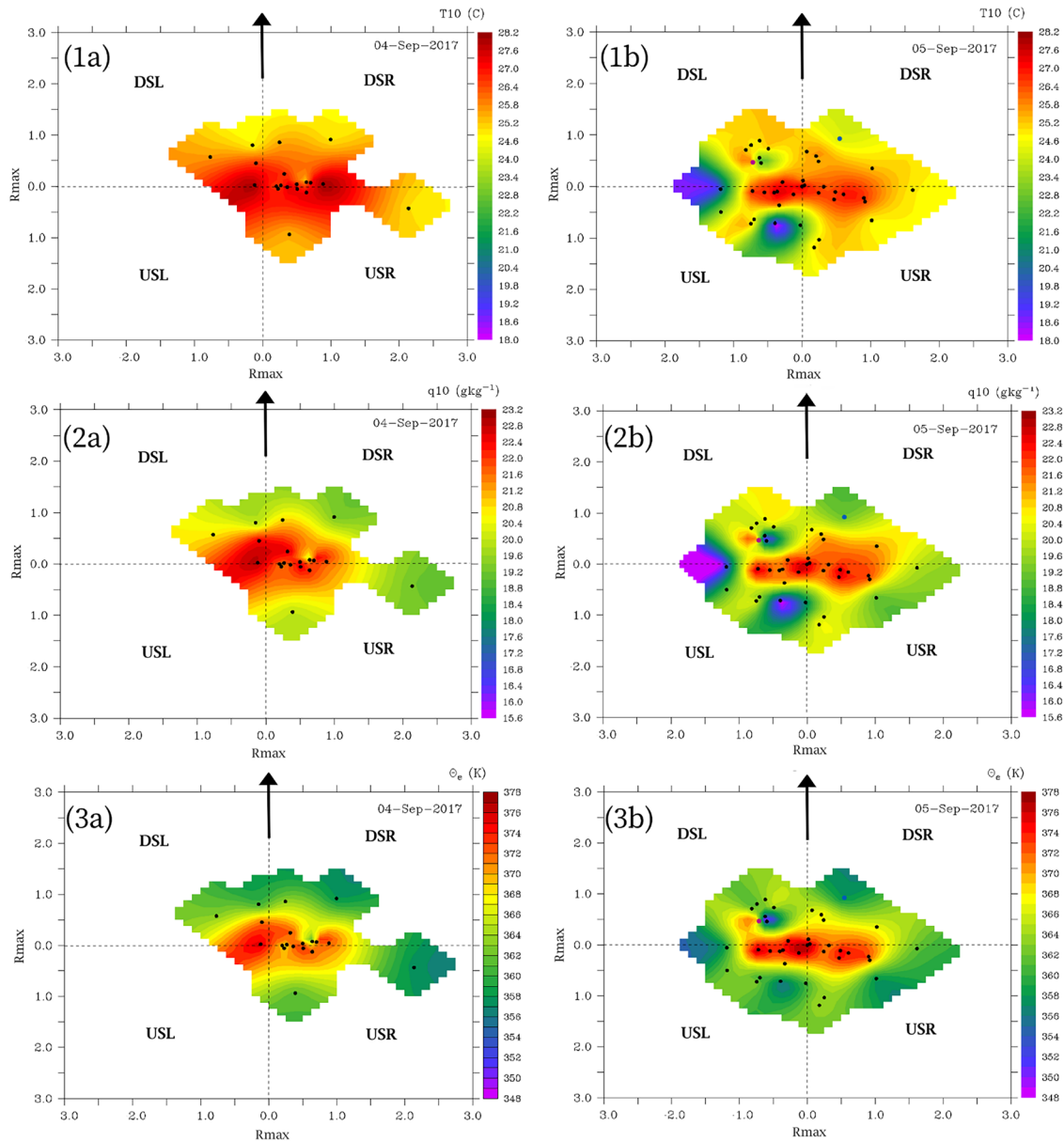
Figure 7. Objectively analyzed (1) 10-m air temperature, (2) specific humidity, and (3) equivalent potential temperature estimated from dropsondes for the pre-RI (column 1) and RI (column 2) time periods in shear-relative coordinates. Dropsonde locations are shown in black circles with the exception of the blue and magenta circles in row 2. These circles correspond to high surface flux locations in Table 3. Direction of shear vector is denoted by black arrow and shear quadrants are listed.

boundary layer dynamics (i.e., eye-eyewall mixing, fluxes from aloft, turbulent eddies), which may aid the intensification process. Hence, it is important to gauge if enhanced θ_E during RI (compared to pre-RI) may have been supported by sufficient air-sea fluxes that were excited by reduced SST cooling over the Amazon-Orinoco River plume region (compared to 1°C cooling in the pre-RI area).

4.3.2. Atmospheric Boundary Layer Recovery of θ_E Through Surface Fluxes

Estimating the increase in θ_E as a result of air-sea fluxes has been done in previous studies using in-storm dropsondes such as those in Irma (Molinari et al., 2013; Wadler et al., 2018; Zhang et al., 2013, 2017). This estimation follows Zhang et al. (2013) to approximate the amount of heat and moisture a parcel would obtain from the sea surface as it travels through the inflow area. This is done by estimating the time rate of change of θ_E within the TC inner-core via estimating the time rate of change of θ and q caused by latent and sensible

heat flux. Equations below are first estimated at every dropsonde point at a level of 50 m (except for the surface flux estimates) and then averaged over the USL to DSR quadrants within 1 R_{max}. The 50-m height is chosen to reduce the influence of surface friction on the trajectory time estimate, and this height has been utilized in past literature (Zhang et al., 2013). Since the pre-RI time period does not have any dropsondes available in the USL quadrant, averages presented for the pre-RI period are obtained over the USR to DSR quadrants, whereas averages for the RI period are obtained over the USL to DSR quadrants. Quadrant averages provided below are presented for context, but are not the actual values used in the following equations since the equations are solved for every dropsonde point then averaged over the quadrants.

Since paired drops of AXBTs and dropsondes (known as double drops) are limited, a simple Laplacian objective analysis (Hankin et al., 2006) is performed on the in-storm AXBT observations (Figure 3) to approximate collocated SST for each dropsonde for both time periods to compute latent and sensible heat fluxes. Quadrant-averaged SST (from Figures 3a and 3b) is approximately 28.0°C for pre-RI and 28.6°C for RI.

Latent and sensible heat fluxes are estimated using Equations 2 and 3. Mean values of T_{10} are 26.8°C (pre-RI) and 25.9°C (RI), mean values of q_{10} are 21.8 g kg^{-1} (pre-RI) and 21.5 g kg^{-1} (RI), and mean values of u_{10} are 14.5 (pre-RI) and 22.4 m s^{-1} (RI). Quadrant-averaged latent and sensible heat fluxes are approximately 190.7 and 54.4 W m^{-2}, respectively, for pre RI, and 505.0 W m^{-2} and 159.3 W m^{-2}, respectively, for RI. Note that these flux values are not instantaneous estimates but are averaged over a spatial area within 1 R_{max} and these averages may be misrepresentative (lower) of intense surface flux occurring in the TC inner-core. For comparison, there are five double drops during the pre-RI and RI time period in which fluxes can be directly estimated from (Table 3). Of these, only two drops are located within the inner core, and they are deployed during the RI time period (see Figure 7 for locations). Total enthalpy fluxes from these two double drops are 1,157.1 and 1,642.7 W m^{-2}, a more accurate representation of intense air-sea transfer occurring during this time period. These estimates are obtained at approximately 1 R_{max} on the DSR and DSL quadrants, respectively.

Changes in q and θ at a given height caused by air-sea fluxes are approximated using

$$\frac{dq}{dt} = \left(-\frac{1}{\rho L_v} \frac{\partial Q_l}{\partial z} \right) = \frac{Q_l}{\rho L_v \Delta z} \tag{8}$$

$$\frac{d\theta}{dt} = \frac{\theta}{C_p T} \left(-\frac{1}{\rho} \frac{\partial Q_s}{\partial z} \right) = \frac{\theta}{C_p T} \frac{Q_s}{\rho \Delta z} \tag{9}$$

where $L_v = 2.5 \times 10^6$ J kg^{-1}, $C_p = 1{,}004$ J kg^{-1} K^{-1}, and $\Delta z = 926$ m for pre-RI and 962 m for RI, (Δz estimation discussed in section 3.2).

Substituting Q_l and Q_s into Equations 8 and 9 along with T_{50} (mean $T_{50} \sim 299.6$ K for pre-RI and 298.8 K for RI) and θ_{50} (mean $\theta_{50} \sim 304.5$ K for pre-RI and 306.3 K for RI) results in a quadrant-averaged change in θ of 0.17 K hr^{-1} for pre-RI and 0.50 K hr^{-1} for RI and a quadrant-averaged change in q of 0.24 g kg^{-1} hr^{-1} for pre-RI and 0.62 g kg^{-1} hr^{-1} for RI.

Applying a logarithmic differentiation to Equation 1 and substituting in Equations 8 and 9, the rate of change in θ_E from latent and sensible heat fluxes is

$$\frac{d\theta_E}{dt} = \frac{\theta_E}{\theta} \frac{d\theta}{dt} + \frac{\theta_E L_v}{C_p T_{LCL}} \frac{dq}{dt} \tag{10}$$

where T_{LCL} is the temperature at the lifting condensation level, estimated using Bolton (1980, eq. 22). Substituting Equations 8 and 9 along with θ_{E50} (mean $\theta_{E50} \sim 369.5$ K for pre-RI and 370.8 K for RI) and T_{LCL} (mean $T_{LCL} \sim 297.8.0$ K for pre-RI and 297.0 K for RI) into Equation 10 results in a quadrant-averaged rate of change of θ_E of 0.95 K hr^{-1} for the pre-RI time period and 2.49 K hr^{-1} for RI.

This simple approach to estimating $\frac{d\theta_E}{dt}$ by averaging the point estimates between quadrants may be sensitive to the amount of dropsonde points available. To provide a range of possible $\frac{d\theta_E}{dt}$ rates, we also regrid the data points using objective analysis (OA) to increase the sample size along a parcel trajectory (Text S5, Figure S3). Using this method results in a rate change of θ_E of 0.77 K hr^{-1} for the pre-RI time period and 4.94 K hr^{-1} for

RI. Note that the pre-RI rates are similar yet the RI rate for this OA method is twice that of the simple averaging approach. This could be due to the fact that the OA method increases the sampling points averaged whereas the simpler approach above has a limited sample of points that are averaged over, indicating that these rates can be sensitive to amount of data used and method utilized. However, both methods indicate that surface fluxes during RI resulted in the rate of change of θ_E to be over 2.5 times larger than pre-RI.

Following Zhang et al. (2013, 2017), these rates are used to estimate the surface enthalpy flux contribution to the observed increase in θ_E as a parcel travels from upshear to downshear quadrants. This estimation signifies if surface fluxes play an important role in the modulation of moist entropy (via θ_E) in the boundary layer and, thus convection, in the downshear quadrants. Because there is no information on the air parcel trajectory, to approximate the surface flux contribution to the rate of θ_E change, we use the assumption that an air parcel does not have a vertical displacement as it travels; it travels on an isoheight, cyclonically, from USR to DSR. This estimation assumes that parcels follow a smooth, tangential trajectory, which is not the case in a realistic turbulent, boundary layer with eyewall asymmetries. This assumption imposes that the most direct path will have the least distance (and time) of other possible solutions and, thus, creates a lower bound of θ_E change of an air parcel.

A simple calculation of time = distance/speed is used to estimate inner-core parcel trajectory. The R_{max} (27.8 km at both pre-RI and RI) is used to calculate the eyewall circumference and this length (L) is divided into four quadrants to get "distance" for each quadrant. Since rate of change of θ_E for pre-RI is estimated from USR to DSR (two quadrants), the length L is multiplied by two to get total distance, whereas for RI, the length scale is multiplied by 3 (three quadrants from USL to DSR). Average 50-m tangential wind speeds from the quadrants are used as the "speed" to estimate trajectory time. As stated previously, with the assumptions used in this time estimate, this time could be considered an lower limit for trajectory transport (given the ideal route), resulting in the θ_E increases described below as an lower bound of possible estimates, given different trajectory times.

During the pre-RI time period, an air parcel would take approximately 25 min to travel from USR to DSR given a mean 50-m tangential wind speed of 58.2 m s^{-1}. This suggests that θ_E increases by 0.32 to 0.40 K in this time period (dependent on rate) solely based on surface fluxes. However, quadrant-averaged θ_{E50} estimated from observations actually decreases ~3 K from USR to DSR. Since the estimated increase in θ_E from surface fluxes (Equation 10) is fairly small, it is possible that phenomena above the boundary layer (convective downdrafts, inner-core dynamics, etc.) resulted in a stronger negative tendency in boundary layer θ_E than surface fluxes could recover, resulting in the observed decrease. Another possibility for the sign difference between estimated and observed θ_E tendency could be the overestimation of θ_E increase from theory because of limited observations. An overestimation of θ_E increase for the pre-RI time period could be a result of not having data coverage to compute the average over the USL quadrant.

For the RI time period, an air parcel would take approximately 30 min to travel from USL to DSR given a mean 50-m tangential wind speed of 72.0 m s^{-1}. This results in an increase of θ_E by 1.25 to 2.47 K during RI (dependent on rate) based exclusively on surface fluxes. Quadrant-averaged θ_{E50} estimated from observations increases by ~1 K from USL to DSR. Since the increases estimated by Equation 10 using both methods are larger than the observed increase in θ_E, this suggests that enthalpy fluxes were energetic enough to aid in boundary layer recovery and enhance inner-core moist entropy.

The boundary layer recovery analysis indicates that surface fluxes were adequate to support the warming of θ_E observed from USL to DSR during the RI period compared to estimations in the pre-RI period. The fact that the rate of change in θ_E from surface fluxes is over 2.5 times larger during RI than pre-RI using both methods and these energetic surface fluxes during RI were supported by minimal SST cooling over the Amazon-Orinoco River plume, indicates that the salinity-stratified river plume waters play an vital role in the sea-to-air transfer of heat and moisture and the modulation of boundary layer thermodynamics, especially during RI.

4.3.3. Influence of Salinity Stratification on Intensity Through Air-Sea Interaction

Upper ocean density stratification has been shown to influence mixing efficiency and SST response during strong wind forcing (Rudzin et al., 2018), which helps sustain favorable air-sea flux during TC passage (Rudzin et al., 2019). Many statistical and modeling studies have indicated that salinity stratification

Table 6

The Difference Between Observed V_{max} Between RI Period at 5 September 18Z and the Pre-RI period at 4 September 18Z (Observed ΔV_{max}), the Difference in Potential Intensity Between the RI and Pre-RI Period (ΔPI), and the Difference in Dynamical Potential Intensity Between the RI and Pre-RI Period (ΔDPI), All in Units of m s^{-1}

	Observed ΔV_{max}	ΔPI	ΔDPI
Powell et al., 2003			25.7
Donelan et al., 2004			22.8
Jarosz et al., 2007	22.1	19.9	22.6
Soloviev & Lukas, 2010			21.9
Bell et al., 2012			22.3
Donelan, 2018			22.3

influences TC intensification through these mechanisms (Androulidakis et al., 2016; Balaguru et al., 2012; Domingues et al., 2015; Ffield, 2007; Hernandez et al., 2016; Newinger & Toumi, 2015; Reul et al., 2014; Vincent et al., 2014; Vissa et al., 2013; Yan et al., 2017). Hence, it is important to understand the influence of the strong observed upper ocean salinity stratification (Figure 6b) on Irma's intensity during its RI in comparison to pre-RI to fully connect oceanic boundary layer processes, atmospheric boundary layer processes, and TC intensity. Subsurface ocean structure is examined using formulations proposed by Balaguru et al. (2015), to identify the sensitivity of hurricane intensity to density stratification compared to other parameters within the PI formulation, such as momentum flux and SST. As discussed previously, dynamic potential intensity (DPI) is similar to potential intensity (PI; Emanuel, 1986, 1995) except that it uses column-integrated ocean temperature based on a predictive mixing length that has information about ocean density stratification and momentum flux. Hence, it should provide a more intuitive ocean surface temperature based on both TC and ocean background information to estimate TC potential intensity.

The pre-storm AXBT profile in Figure 5 is used to estimate DPI for the pre-RI period (Table 4) and the pre-storm temperature and salinity profiles from ALAMO float 9134 (2017090509Z; Figures 6a and 6b) are used to estimate DPI for the RI period (Table 5). Since there are no accompanying salinity observations to AXBT temperature profiles during the pre-RI period, a climatological salinity profile is obtained from the World Ocean Atlas 2013 (Zweng et al., 2013) for the month of September within 0.25° of the AXBT profile. Since the DPI formulation is sensitive to momentum flux (via surface friction velocity, u_*, Equation 5), Tables 4 and 5 lists how each term within DPI is sensitive to prescribed momentum drag coefficients reported in literature.

Several interesting findings arise from intercomparisons among drag coefficients and stratification strength to cross-comparisons between pre-RI and RI periods. Regarding both pre-RI and RI periods, there is ~0.4°C to 0.5°C of variance in T_{dy} just from using different drag coefficients and not changing the background ocean density information. In both Tables 4 and 5, the lowest value of C_D (Soloviev & Lukas, 2010) results in the closest T_{dy} to observed in-storm SST, resulting in DPI and PI being most similar. Changes in T_{dy} modulate both the efficiency and enthalpy terms in the formulation.

The sensitivity of T_{dy} to the stratification term, α, is also estimated to examine how reduced stratification impacts T_{dy} relative to momentum flux (Tables 4 and 5). In both pre-RI and RI periods, reducing the stratification term by half results in L_{pred} being deeper than those using observed stratification by 7 to 12 m, depending on C_D, and more a noticeable difference between T_{dy} and in-storm SST. Values of T_{dy} are slightly cooler when using half stratification compared to those for observed stratification, differences on the order of 0.2°C for the pre-RI period to 0.3°C for the RI period. Cooler T_{dy} results in lower DPIs of 4–5 m s^{-1} for the pre-RI period and 3–4 m s^{-1} for the RI period, compared to those from observed stratification in Tables 4 and 5, respectively. Note that the variance in T_{dy} between changing the drag coefficient (holding α constant) and the stratification (between the same C_D) are approximately the same. This indicates that the T_{dy} in this formulation is as sensitive to the prescribed salinity stratification as it is to the drag coefficient.

Moreover, the implicit influence of strong subsurface salinity stratification on ocean mixing and TC intensity is most apparent when comparing values of L_{pred}, T_{dy}, and DPI between pre-RI and RI periods. The values of L_{pred} for pre-RI are deeper than those at each drag coefficient experiment compared to RI, even though the surface friction velocity is stronger during RI than pre-RI. This results in cooler T_{dy} for pre-RI and lower values of DPI, compared to the RI period. This highlights that subsurface salinity stratification where Irma underwent RI reduced mixing efficiency depth, limiting the entrainment of cool waters, which helps sustain DPI in this context.

Table 6 presents the differences in PI and DPI between the pre-RI and RI periods compared to the observed rate of RI to put these findings in context of Irma's actual RI rate since DPI and PI are based on theory. The observed rate of RI between 4 Sept 2017 18Z (pre-RI) and 5 Sept 2017 18Z (RI) is 22.1 m s^{-1} over a 24-hr

period, whereas the change in DPI between the pre-RI and RI period (24-hr period) ranges from 21.9 to 25.7 m s^{-1}, based on C_D. The difference in PI between the pre-RI and RI period is 19.9 m s^{-1}. Hence, the DPI estimates presented here capture Irma's rate of rapid intensification and further justify that the implicit influence of salinity stratification in the Amazon-Orinoco River plume region reduced the in-storm SST cooling during the RI compared to pre-RI and facilitated Irma's intensity during RI.

These findings also link those in sections 4.1, 4.3.2, and 4.3.3 such that salinity stratification reduces SST cooling sustaining intense surface flux, increasing boundary layer moist entropy. Reduced SST cooling and intense surface fluxes would result in intensification (based on PI theory). Note that both estimations of DPI and PI still do not fully capture V_{max} at the observed time period (Table 4). Uncertainty error exists in exchange coefficients and in situ observation errors of temperature and moisture. However, if we tweak the parameters within the DPI/PI calculations to include implicit errors, DPI/PI = V_{max} is achieved. For example, changing the C_K/C_D ratio to 1.2 instead of 1 results in a PI in the RI region to be ~82.5 m s^{-1} compared to V_{max} of 82.2 m s^{-1}. Another example is to decrease the values of q_{10a} and T_{10a} by 0.0008 g kg^{-1} and 1°C, respectively, which results in a PI = 82.6 m s^{-1}.

5. Summary and Limitations

Extensive atmospheric and oceanic observations obtained before and during Irma's RI over the Amazon-Orinoco River plume region were used to understand the influence of subsurface salinity stratification on air-sea interaction and atmospheric boundary layer response and how it relates to TC intensity. Novel aircraft-deployed oceanic profiling floats highlight the detailed evolution of the ocean response during Irma's passage over the Amazon-Orinoco River plume that has not been documented in literature prior to Sanabia and Jayne (2020). Moreover, the coupling between TC-induced ocean response over this river plume and corresponding TC atmospheric boundary layer response has also been absent in literature.

Subsurface temperature measurements from AXBTs during pre-RI showed SST cooling of up to 1°C just outside of the river plume. As Irma underwent RI over the river plume, ALAMO floats measured a marginal SST response during TC passage. Subsurface salinity measurements indicate the presence of a strongly stratified barrier layer over the area that Irma underwent RI with Brunt-Väisälä frequencies upwards of 30 cph. Subsurface measurements from ALAMO floats suggest that enhanced SST cooling did not occur because the barrier layer and salinity stratification did not erode during TC passage, restricting entrainment. Near-inertial oscillations eventually erode the barrier layer and significant SST cooling commences after the TC has already passed.

Ten-meter variables of temperature, moisture, and θ_E were referenced with respect to the deep-layer wind shear direction to investigate the differences in boundary layer thermodynamics between the pre-RI and RI time periods where ocean responses varied greatly. Overall, inner-core variables had similar spatial patterns but inner-core θ_{E10} was approximately 6 K warmer during RI compared to pre-RI, even though relatively more low entropy intrusions occurred during RI.

A boundary layer recovery analysis was conducted to investigate whether air-sea fluxes were energetic enough to support the dramatic change in θ_E from pre-RI to RI, recover the boundary layer from the observed downdrafts, and help facilitate RI. Using a method from Zhang et al. (2013, 2017), the rate of change of θ_E caused solely by surfaces fluxes was not only sufficient enough to support boundary layer recovery during RI compared to pre-RI, but the rate of change of θ_E during RI was at least 2.5 times larger than pre-RI, depending on trajectory method used. This finding along with the latter ocean analyses indicate that reduced ocean response in the RI region supported energetic air-sea fluxes that aided in the boundary layer recovery of θ_E, even with evidence of cool, dry downdrafts, which may have assisted Irma's RI.

The latter finding is further supported when examining TC DPI sensitivity between the two main contributors in the DPI formulation, momentum flux and stratification, between the pre-RI and RI periods. Results indicate that salinity stratification affects the depth of mixing during TC passage, sustaining depth-integrated temperature, influencing TC potential intensity by modulating both the efficiency and enthalpy terms. The variance among T_{dy} when using difference values of drag coefficient versus two stratification strengths is approximately the same order. Reducing the stratification term within DPI results in a larger difference between estimated T_{dy} and observed in-storm SST as well as a cooler T_{dy} compared to

observed stratification. Reduction in stratification causes DPI to be 3–5 m s^{-1} less than using observed stratification, demonstrating stratifications' implicit influence on TC potential intensity. Comparing pre-RI and RI periods indicates that the surface stratification observed where Irma underwent RI reduced mixing depth compared to the pre-RI region, even though wind forcing was stronger during the RI period. It is found that the change in DPI between the pre-RI and RI period captures the observed rate of Irma's RI, directly relating the implicit influence of subsurface salinity structure to Irma's intensity during RI.

Overall, the findings suggest that the salinity stratification within the Amazon-Orinoco River plume sustained SST during Irma's passage, which promoted energetic air-sea fluxes that aided in the boundary layer recovery of θ_E and facilitated Irma's intensity during RI. These results support previous findings in Rudzin et al. (2019) in which the authors also documented energetic air-sea fluxes during the RI of several TCs over the Amazon-Orinoco River plume which were facilitated by reduced SST cooling. However, a number of assumptions were made within the current analyses that also limit these findings. Since there were no subsurface velocity measurements available for the pre-RI and RI regions, a full ocean mixed layer heat budget cannot be computed to conclude indubitably that stratification was the key mechanism controlling SST response in the plume region rather than outside ocean dynamics (i.e., advection). However, based on the temperature, salinity, and density evolution presented here compared to previous literature, there is strong evidence to suspect that salinity-stratification was the most important factor in the SST response observed.

The boundary layer recovery analysis assumes that the data used within the analyses is occurring at one snapshot in time whereas the dropsonde data used is obtained over the course of 1 day. Additionally, data are averaged over each quadrant to get the rate of change estimates provided within the results. As stated in section 4.3, grouping the dropsondes per shear-relative quadrant allows for comparison of thermodynamic properties in each quadrant between these two events, even with lower temporal coverage. Additionally, the boundary layer recovery method (1) assumes that fluxes vary linearly with height from the ocean surface to the top of the atmospheric boundary layer and (2) estimates the recovery of θ_E averaged over the entire boundary layer depth, rather than on a realistic trajectory. We note that this estimate may be dependent on number of data points within the average and how the averaging occurs. More realistic back trajectories would benefit from utilizing vertical velocity estimates from dual-Doppler radar. Unfortunately, the research flights during Irma were not low enough to obtain boundary layer estimates of vertical velocity. While the methods presented in this study provide a rough estimate of boundary layer recovery, it has been performed before in previous studies using a composite of data from different TCs and the results found here are on the order of those in past literature.

Finally, it should be mentioned that this study investigates just one paradigm of RI and it is not the goal of this study to do a full evaluation of Irma's RI. Hence, we make no attempt at justifying that our findings are the absolute cause of RI. Other contributors of RI from past studies that are not considered are the low deep vertical wind shear that Irma was under (24-hr average of 2.3 and 2.4 m s^{-1} for pre-RI and RI, respectively), which is very important predictor of RI (e.g., DeMaria, 1996; Onderlinde & Nolan, 2017; Paterson et al., 2005; Riemer et al., 2010; Wong & Chan, 2004), precipitation asymmetry (Rogers et al., 2016; Zawislak et al., 2016), environmental moisture (Ge et al., 2013; Tao & Zhang, 2014), and upper-level divergence (e.g., Gray, 1968; Kaplan et al., 2010). The boundary layer recovery analysis presented is not intended to prove or disprove the TC intensification theory proposed by Zhang et al. (2013, 2017). Future coupled modeling studies are needed to shed light onto how favorable ocean conditions contribute to TC RI.

Data Availability Statement

ALAMO float data can be acquired through Woods Hole Oceanographic Institute (http://argo.whoi.edu/alamo/). AXBT data are available at: https://data.nodc.noaa.gov/cgi-bin/iso?id=gov.noaa.nodc:0209221. GPS-dropsonde data are provided courtesy of the NOAA/AOML/Hurricane Research Division in Miami, FL and be accessed at https://www.aoml.noaa.gov/hrd/Storm_pages/irma2017/sonde.html. SHIPS data can be accessed at http://rammb.cira.colostate.edu/research/tropical_cyclones/ships/index.asp. The Group for High Resolution Sea Surface Temperature (GHRSST) Multi-scale Ultra-high Resolution (MUR) SST data were obtained from the NASA EOSDIS Physical Oceanography Distributed Active Archive Center (PO.DAAC) at the Jet Propulsion Laboratory, Pasadena, CA (https://doi.org/10.5067/GHGMR-4FJ01). The L3_DEBIAS_LOCEAN_v3 SSS data are obtained from LOCEAN/IPSL (UMR CNRS/UPMC/

IRD/MNHN) laboratory and ACRI-st company that participate to the Ocean Salinity Expertise Center (CECOS) of Centre Aval de Traitement des Donnees SMOS (CATDS). This product is distributed by the Ocean Salinity Expertise Center (CECOS) of the CNES-IFREMER Centre Aval de Traitement des Donnees SMOS (CATDS), at IFREMER, Plouzane (France) and the data are located online (https://www.catds.fr/Products/Available-products-fromCEC-OS/CEC-Locean-L3-Debiased-v3). Functions to estimate PI and DPI can be found online (https://doi.org/10.5281/zenodo.3774162).

References

Androulidakis, Y., Kourafalou, V., Halliwell, G., Le Hénaff, M., Kang, H., Mehari, M., & Atlas, R. (2016). Hurricane interaction with the upper ocean in the Amazon-Orinoco plume region. *Ocean Dynamics*, *66*(12), 1559–1588. https://doi.org/10.1007/s10236-016-0997-0

Argo (2000). Argo floats data and metadata from Global Data Assembly Centre (Argo GDAC), August 28 2017, Ifremer, https://doi.org/10.12770/1282383d-9b35-4eaa-a9d6-4b0c24c0cfc9

Balaguru, K., Chang, P., Saravanan, R., Leung, L. R., Xu, Z., Li, M., & Hsieh, J.-S. (2012). Ocean barrier layers' effect on tropical cyclone intensification. *Proceedings of the National Academy of Sciences*, *109*(36), 14343 LP-14347. https://doi.org/10.1073/pnas.1201364109

Balaguru, K., Foltz, G. R., Leung, L. R., Asaro, E. D., Emanuel, K. A., Liu, H., & Zedler, S. E. (2015). Dynamic potential intensity: An improved representation of the ocean's impact on tropical cyclones. *Geophysical Research Letters*, *42*, 6739–6746. https://doi.org/10.1002/2015GL064822

Bell, M. M., Montgomery, M. T., & Emanuel, K. A. (2012). Air–sea enthalpy and momentum exchange at major hurricane wind speeds observed during CBLAST. *Journal of the Atmospheric Sciences*, *69*(11), 3197–3222. https://doi.org/10.1175/JAS-D-11-0276.1

Bolton, D. (1980). The computation of equivalent potential temperature. *Monthly Weather Review*, *108*(7), 1046–1053. https://doi.org/10.1175/1520-0493(1980)108%3C1046:TCOEPT%3E2.0.CO;2

Boutin, J., Vergely, J. L., Marchand, S., D'Amico, F., Hasson, A., Kolodziejczyk, N., et al. (2018). New SMOS sea surface salinity with reduced systematic errors and improved variability. *Remote Sensing of Environment*, *214*, 115–134. https://doi.org/10.1016/J.RSE.2018.05.022

Buck, A. L. (1981). New equations for computing vapor pressure and enhancement factor. *Journal of Applied Meteorology*, *20*(12), 1527–1532. https://doi.org/10.1175/1520-0450(1981)020%3C1527:NEFCVP%3E2.0.CO;2

Cangialosi, J. P., Latto, A. S., & Berg, R. (2018). National Hurricane Center Tropical Cyclone Report—Hurricane Irma (AL112017) 30 August–12 September 2017, (September 2017). https://www.nhc.noaa.gov/data/tcr/AL112017_Irma.pdf

Cheng, C.-J., & Wu, C.-C. (2018). The role of WISHE in secondary eyewall formation. *Journal of the Atmospheric Sciences*, *75*(11), 3823–3841. https://doi.org/10.1175/JAS-D-17-0236.1

Chi, N.-H., Lien, R.-C., D'Asaro, E. A., & Ma, B. B. (2014). The surface mixed layer heat budget from mooring observations in the central Indian Ocean during Madden–Julian Oscillation events. *Journal of Geophysical Research: Oceans*, *119*, 4638–4652. https://doi.org/10.1002/2014JC010192

Cione, J. J., Black, P. G., & Houston, S. H. (2000). Surface observations in the hurricane environment. *Monthly Weather Review*, *128*(5), 1550–1561. https://doi.org/10.1175/1520-0493(2000)128%3C1550:SOITHE%3E2.0.CO;2

Corbosiero, K. L., & Molinari, J. (2003). The relationship between storm motion, vertical wind shear, and convective asymmetries in tropical cyclones. *Journal of the Atmospheric Sciences*, *60*(2), 366–376. https://doi.org/10.1175/1520-0469(2003)060%3C0366:TRBSMV%3E2.0.CO;2

de Boyer Montégut, C., Mignot, J., Lazar, A., & Cravatte, S. (2007). Control of salinity on the mixed layer depth in the world ocean: 1. General description. *Journal of Geophysical Research*, *112*(C6). https://doi.org/10.1029/2006JC003953

Dee, D. P., Uppala, S. M., Simmons, A. J., Berrisford, P., Poli, P., Kobayashi, S., et al. (2011). The ERA-Interim reanalysis: Configuration and performance of the data assimilation system. *Quarterly Journal of the Royal Meteorological Society*, *137*(656), 553–597. https://doi.org/10.1002/qj.828

DeMaria, M. (1996). The effect of vertical shear on tropical cyclone intensity change. *Journal of the Atmospheric Sciences*, *53*(14), 2076–2088. https://doi.org/10.1175/1520-0469(1996)053%3C2076:TEOVSO%3E2.0.CO;2

DeMaria, M., Mainelli, M., Shay, L. K., Knaff, J. A., & Kaplan, J. (2005). Further improvements to the statistical hurricane intensity prediction scheme (SHIPS). *Bulletin of the American Meteorological Society*, *20*(4), 531–543. https://doi.org/10.1175/WAF862.1

Dinegar Boyd, J. (1987). Improved depth and temperature conversion equations for sippican AXBTs. *Journal of Atmospheric and Oceanic Technology*, *4*(3), 545–551. https://doi.org/10.1175/1520-0426(1987)004<0545:idatce>2.0.co;2

Domingues, R., Goni, G., Bringas, F., Lee, S.-K., Kim, H.-S., Halliwell, G., et al. (2015). Upper ocean response to Hurricane Gonzalo (2014): Salinity effects revealed by targeted and sustained underwater glider observations. *Geophysical Research Letters*, *42*, 7131–7138. https://doi.org/10.1002/2015GL065378

Donelan, M. A. (2018). On the decrease of the oceanic drag coefficient in high winds. *Journal of Geophysical Research: Oceans*, *123*, 1485–1501. https://doi.org/10.1002/2017JC013394

Donelan, M. A., Haus, B. K., Reul, N., Plant, W. J., Stiassnie, M., Graber, H. C., et al. (2004). On the limiting aerodynamic roughness of the ocean in very strong winds. *Geophysical Research Letters*, *31*, L18306. https://doi.org/10.1029/2004GL019460

Emanuel, K. A. (1986). An air-sea interaction theory for tropical cyclones. Part I: Steady-state maintenance. *Journal of the Atmospheric Sciences*, *43*(6), 585–605. https://doi.org/10.1175/1520-0469(1986)043%3C0585:AASITF%3E2.0.CO;2

Emanuel, K. A. (1995). Sensitivity of tropical cyclones to surface exchange coefficients and a revised steady-state model incorporating eye dynamics. *Journal of the Atmospheric Sciences*, *52*(22), 3969–3976. https://doi.org/10.1175/1520-0469(1995)052<3969:sotcts>2.0.co;2

Emanuel, K. A. (1999). Thermodynamic control of hurricane intensity. *Nature*, *401*(6754), 665. Retrieved from–669. https://www.nature.com/articles/44326.pdf?origin=ppub, https://doi.org/10.1038/44326

Ffield, A. (2007). Amazon and Orinoco River plumes and NBC rings: Bystanders or participants in hurricane events? *Journal of Climate*, *20*(2), 316–333. https://doi.org/10.1175/JCLI3985.1

Frank, W. M., & Ritchie, E. A. (2001). Effects of vertical wind shear on the intensity and structure of numerically simulated hurricanes. *Monthly Weather Review*, *129*(9), 2249–2269. https://doi.org/10.1175/1520-0493(2001)129%3C2249:EOVWSO%3E2.0.CO;2

Ge, X., Li, T., & Peng, M. (2013). Effects of vertical shears and midlevel dry air on tropical cyclone developments. *Journal of the Atmospheric Sciences*, *70*(12), 3859–3875. https://doi.org/10.1175/JAS-D-13-066.1

Geisler, J. E. (1970). Linear theory of the response of a two layer ocean to a moving hurricane. *Geophysical Fluid Dynamics*, *1*(1–2), 249–272. https://doi.org/10.1080/03091927009365774

Gray, W. M. (1968). Global view of the origin of tropical disturbances and storms. *Monthly Weather Review*, *96*(10), 669–700. https://doi.org/10.1175/1520-0493(1968)096%3C0669:GVOTOO%3E2.0.CO;2

Greatbatch, R. J. (1983). On the response of the ocean to a moving storm: The nonlinear dynamics. *Journal of Physical Oceanography*, *13*(3), 357–367. https://doi.org/10.1175/1520-0485(1983)013%3C0357:OTROTO%3E2.0.CO;2

Hankin, S., Callahan, J., Manke, A., O'Brien, K., & Li, J. (2006). *Ferret user's guide version 6.0*. Seattle, WA: NOAA/Pacific Marine Environmental Laboratory.

Haus, B. K., Jeong, D., Donelan, M. A., Zhang, J. A., & Savelyev, I. (2010). Relative rates of sea-air heat transfer and frictional drag in very high winds. *Geophysical Research Letters*, *37*, L07802. https://doi.org/10.1029/2009GL042206

Hernandez, O., Jouanno, J., & Durand, F. (2016). Do the Amazon and Orinoco freshwater plumes really matter for hurricane-induced ocean surface cooling? *Journal of Geophysical Research: Oceans*, *121*, 2119–2141. https://doi.org/10.1002/2015JC011021

Hlywiak, J., & Nolan, D. S. (2019). The influence of oceanic barrier layers on tropical cyclone intensity as determined through idealized, coupled numerical simulations. *Journal of Physical Oceanography*, *49*(7), 1723–1745. https://doi.org/10.1175/jpo-d-18-0267.1

Hock, T. F., & Franklin, J. L. (1999). The NCAR GPS Dropwindsonde. *Bulletin of the American Meteorological Society*, *80*(3), 407–420. https://doi.org/10.1175/1520-0477(1999)080<0407:TNGD>2.0.CO;2

Huffman, G. , Bolvin, D., Braithwaite, D., Hsu, K., Joyce, R., & Xie, P. (2014). Integrated Multi-satellitE Retrievals for GPM (IMERG) final precipitation L3 half hourly 0.1 degree × 0.1 degree, version 5. NASA's Precipitation Processing Center, accessed 11 March, *2020*, https://doi.org/10.5067/GPM/IMERG/3B-HH/05

Jacob, S. D., & Koblinsky, C. J. (2007). Effects of precipitation on the upper-ocean response to a hurricane. *Monthly Weather Review*, *135*(6), 2207–2225. https://doi.org/10.1175/MWR3366.1

Jaimes, B., & Shay, L. K. (2009). Mixed layer cooling in mesoscale oceanic eddies during Hurricanes Katrina and Rita. *Monthly Weather Review*, *137*(12), 4188–4207. https://doi.org/10.1175/2009MWR2849.1

Jaimes, B., & Shay, L. K. (2010). Near-inertial wave wake of Hurricanes Katrina and Rita over mesoscale oceanic eddies. *Journal of Physical Oceanography*, *40*(6), 1320–1337. https://doi.org/10.1175/2010JPO4309.1

Jaimes, B., & Shay, L. K. (2015). Enhanced wind-driven downwelling flow in warm oceanic eddy features during the intensification of tropical cyclone Isaac (2012): Observations and theory. *Journal of Physical Oceanography*, *45*(6), 1667–1689. https://doi.org/10.1175/JPO-D-14-0176.1

Jaimes, B., Shay, L. K., & Uhlhorn, E. W. (2015). Enthalpy and momentum fluxes during hurricane earl relative to underlying ocean features. *Monthly Weather Review*, *143*(1), 111–131. https://doi.org/10.1175/MWR-D-13-00277.1

Jarosz, E., Mitchell, D. A., Wang, D. W., & Teague, W. J. (2007). Bottom-up determination of air-sea momentum exchange under a major tropical cyclone. *Science*, *315*(5819), 1707–1709. https://doi.org/10.1126/science.1136466

Jayne, S. R., & Bogue, N. M. (2017). Air-deployable profiling floats. *Oceanography*, *30*(2), 29–31.

JPL MUR MEaSUREs Project (2010). GHRSST Level 4 MUR Global Foundation Sea Surface Temperature Analysis. Ver. 2. PO.DAAC, CA, USA. Dataset accessed at https://doi.org/10.5067/GHGMR-4FJ01

Kaplan, J., DeMaria, M., & Knaff, J. A. (2010). A revised tropical cyclone rapid intensification index for the Atlantic and eastern North Pacific basins. *Weather and Forecasting*, *25*(1), 220–241. https://doi.org/10.1175/2009WAF2222280.1

Leipper, D. F., & Volgenau, D. (1972). Hurricane heat potential of the Gulf of Mexico. *Journal of Physical Oceanography*, *2*(3), 218–224. https://doi.org/10.1175/1520-0485(1972)002%3C0218:HHPOTG%3E2.0.CO;2

Lin, I.-I., Wu, C.-C., Emanuel, K. A., Lee, I.-H., Wu, C.-R., & Pun, I.-F. (2005). The interaction of Supertyphoon Maemi (2003) with a warm ocean Eddy. *Monthly Weather Review*, *133*(9), 2635–2649. https://doi.org/10.1175/MWR3005.1

Lukas, R., & Lindstrom, E. (1991). The mixed layer of the western equatorial Pacific Ocean. *Journal of Geophysical Research*, *96*(S01), 3343–3357. https://doi.org/10.1029/90JC01951

Malkus, J. S., & Riehl, H. (1960). On the dynamics and energy transformations in steady-state hurricanes. *Tellus*, *12*(1), 1–20. https://doi.org/10.3402/tellusa.v12i1.9351

McPhaden, M. J., & Foltz, G. R. (2013). Intraseasonal variations in the surface layer heat balance of the central equatorial Indian Ocean: The importance of zonal advection and vertical mixing. *Geophysical Research Letters*, *40*, 2737–2741. https://doi.org/10.1002/grl.50536

Mignot, J., Lazar, A., & Lacarra, M. (2012). On the formation of barrier layers and associated vertical temperature inversions: A focus on the northwestern tropical Atlantic. *Journal of Geophysical Research*, *117*, C02010. https://doi.org/10.1029/2011JC007435

Molinari, J., Frank, J., & Vollaro, D. (2013). Convective bursts, downdraft cooling, and boundary layer recovery in a sheared tropical storm. *Monthly Weather Review*, *141*(3), 1048–1060. https://doi.org/10.1175/MWR-D-12-00135.1

Murthy, V. S., & Boos, W. R. (2018). Role of surface enthalpy fluxes in idealized simulations of tropical depression spinup. *Journal of the Atmospheric Sciences*, *75*(6), 1811–1831. https://doi.org/10.1175/JAS-D-17-0119.1

Newinger, C., & Toumi, R. (2015). Potential impact of the colored Amazon and Orinoco plume on tropical cyclone intensity. *Journal of Geophysical Research: Oceans*, *120*, 1296–1317. https://doi.org/10.1002/2014JC010533

Onderlinde, M. J., & Nolan, D. S. (2017). The tropical cyclone response to changing wind shear using the method of time-varying point-downscaling. *Journal of Advances in Modeling Earth Systems*, *9*, 908–931. https://doi.org/10.1002/2016MS000796

Pailler, K., Bourlès, B., & Gouriou, Y. (1999). The barrier layer in the western tropical Atlantic Ocean. *Geophysical Research Letters*, *26*(14), 2069–2072. https://doi.org/10.1029/1999GL900492

Paterson, L. A., Hanstrum, B. N., Davidson, N. E., & Weber, H. C. (2005). Influence of environmental vertical wind shear on the intensity of hurricane-strength tropical cyclones in the Australian region. *Monthly Weather Review*, *133*(12), 3644–3660. https://doi.org/10.1175/MWR3041.1

Powell, M. D. (1990). Boundary layer structure and dynamics in outer hurricane rainbands. Part II: Downdraft modification and mixed layer recovery. *Monthly Weather Review*, *118*(4), 918–938. https://doi.org/10.1175/1520-0493(1990)118%3C0918:BLSADI%3E2.0.CO;2

Powell, M. D., Vickery, P. J., & Reinhold, T. A. (2003). Reduced drag coefficient for high wind speeds in tropical cyclones. *Nature*, *422*(6929), 279. Retrieved from–283. https://doi.org/10.1038/nature01481

Price, J. F. (1981). Upper Ocean response to a hurricane. *Journal of Physical Oceanography*, *11*(2), 153–175. https://doi.org/10.1175/1520-0485(1981)011%3C0153:UORTAH%3E2.0.CO;2

Price, J. F. (1983). Internal wave wake of a moving storm. Part I. Scales, energy budget and observations. *Journal of Physical Oceanography*, *13*(6), 949–965. https://doi.org/10.1175/1520-0485(1983)013%3C0949:IWWOAM%3E2.0.CO;2

Price, J. F., Weller, R. A., & Pinkel, R. (1986). Diurnal cycling: Observations and models of the upper ocean response to diurnal heating, cooling, and wind mixing. *Journal of Geophysical Research*, *91*(C7), 8411–8427. https://doi.org/10.1029/JC091iC07p08411

Reasor, P. D., Montgomery, M. T., Marks, F. D. Jr., & Gamache, J. F. (2000). Low-wavenumber structure and evolution of the hurricane inner core observed by airborne dual-Doppler radar. *Monthly Weather Review*, *128*(6), 1653–1680. https://doi.org/10.1175/1520-0493(2000)128%3C1653:LWSAEO%3E2.0.CO;2

Reul, N., Quilfen, Y., Chapron, B., Fournier, S., Kudryavtsev, V., & Sabia, R. (2014). Multisensor observations of the Amazon-Orinoco river plume interactions with hurricanes. *Journal of Geophysical Research: Oceans*, *119*, 8271–8295. https://doi.org/10.1002/2014JC010107

Riemer, M., Montgomery, M. T., & Nicholls, M. E. (2010). A new paradigm for intensity modification of tropical cyclones: Thermodynamic impact of vertical wind shear on the inflow layer. *Atmospheric Chemistry and Physics*, *10*(7), 3163–3188. https://doi.org/10.5194/acp-10-3163-2010

Rogers, R., Chen, S., Tenerelli, J., & Willoughby, H. (2003). A numerical study of the impact of vertical shear on the distribution of rainfall in Hurricane Bonnie (1998). *Monthly Weather Review*, *131*(8), 1577–1599. https://doi.org/10.1175/2546.1

Rogers, R. F., Zhang, J. A., Zawislak, J., Jiang, H., Alvey, G. R., Zipser, E. J., & Stevenson, S. N. (2016). Observations of the structure and evolution of Hurricane Edouard (2014) during intensity change. Part II: Kinematic structure and the distribution of deep convection. *Monthly Weather Review*, *144*(9), 3355–3376. https://doi.org/10.1175/mwr-d-16-0017.1

Rudzin, J. E., Shay, L. K., Jaimes, B., & Brewster, J. K. (2017). Upper ocean observations in eastern Caribbean Sea reveal barrier layer within a warm core eddy. *Journal of Geophysical Research: Oceans*, *122*, 1057–1071. https://doi.org/10.1002/2016JC012339

Rudzin, J. E., Shay, L. K., & Jaimes de la Cruz, B. (2019). The impact of the Amazon–Orinoco River plume on enthalpy flux and air–sea interaction within Caribbean Sea tropical cyclones. *Monthly Weather Review*, *147*(3), 931–950. https://doi.org/10.1175/MWR-D-18-0295.1

Rudzin, J. E., Shay, L. K., & Johns, W. (2018). The influence of the barrier layer on SST response during tropical cyclone wind forcing using idealized experiments. *Journal of Physical Oceanography*, 1471–1478. https://doi.org/10.1175/2010JCLI3851.1

Sampson, C. R., & Schrader, A. J. (2000). The automated tropical cyclone forecasting system (version 3.2). *Bulletin of the American Meteorological Society*, *81*(6), 1231–1240. https://doi.org/10.1175/1520-0477(2000)081%3C1231:TATCFS%3E2.3.CO;2

Sanabia, E. R., Barrett, B. S., Black, P. G., Chen, S., & Cummings, J. A. (2013). Real-time upper-ocean temperature observations from aircraft during operational hurricane reconnaissance missions: AXBT demonstration project year one results. *Weather and Forecasting*, *28*(6), 1404–1422. https://doi.org/10.1175/WAF-D-12-00107.1

Sanabia, E. R., & Jayne, S. R. (2020). Ocean observations under two major hurricanes: Evolution of the response across storm wake. *AGU Advances*. https://doi.org/10.1029/2019AV000161

Schneider, R., & Barnes, G. M. (2005). Low-level kinematic, thermodynamic, and reflectivity fields associated with Hurricane Bonnie (1998) at landfall. *Monthly Weather Review*, *133*(11), 3243–3259. https://doi.org/10.1175/MWR3027.1

Shay, L. K., Elsberry, R. L., & Black, P. G. (1989). Vertical structure of the ocean current response to a hurricane. *Journal of Physical Oceanography*, *19*(5), 649–669. https://doi.org/10.1175/1520-0485(1989)019%3C0649:VSOTOC%3E2.0.CO;2

Shay, L. K., Goni, G. J., & Black, P. G. (2000). Effects of a warm oceanic feature on hurricane opal. *Monthly Weather Review*, *128*(5), 1366–1383. https://doi.org/10.1175/1520-0493(2000)128<1366:eoawof>2.0.co;2

Sitkowski, M., & Barnes, G. M. (2009). Low-level thermodynamic, kinematic, and reflectivity fields of Hurricane Guillermo (1997) during rapid intensification. *Monthly Weather Review*, *137*(2), 645–663. https://doi.org/10.1175/2008MWR2531.1

Soloviev, A., & Lukas, R. (2010). Effects of bubbles and sea spray on air–sea exchange in hurricane conditions. *Boundary-Layer Meteorology*, *136*(3), 365–376. https://doi.org/10.1007/s10546-010-9505-0

Sprintall, J., & Tomczak, M. (1992). Evidence of the barrier layer in the surface layer of the tropics. *Journal of Geophysical Research*, *97*(C5), 7305. https://doi.org/10.1029/92JC00407

Steffen, J., & Bourassa, M. (2018). Barrier layer development local to tropical cyclones based on Argo float observations. *Journal of Physical Oceanography*, *48*(9), 1951–1968. https://doi.org/10.1175/JPO-D-17-0262.1

Tao, D., & Zhang, F. (2014). Effect of environmental shear, sea-surface temperature, and ambient moisture on the formation and predictability of tropical cyclones: An ensemble-mean perspective. *Journal of Advances in Modeling Earth Systems*, *6*, 384–404. https://doi.org/10.1002/2014MS000314

Vincent, E. M., Emanuel, K. A., Lengaigne, M., Vialard, J., & Madec, G. (2014). Influence of upper ocean stratification interannual variability on tropical cyclones. *Journal of Advances in Modeling Earth Systems*, *6*, 680–699. https://doi.org/10.1002/2014MS000327

Vissa, N. K., Satyanarayana, A. N. V., & Kumar, B. P. (2013). Response of upper ocean and impact of barrier layer on Sidr cyclone induced sea surface cooling. *Ocean Science Journal*, *48*(3), 279–288. https://doi.org/10.1007/s12601-013-0026-x

Wada, A., & Chan, J. C. L. (2008). Relationship between typhoon activity and upper ocean heat content. *Geophysical Research Letters*, *35*, L17603. https://doi.org/10.1029/2008GL035129

Wadler, J. B., Zhang, J. A., Jaimes, B., & Shay, L. K. (2018). Downdrafts and the evolution of boundary layer thermodynamics in Hurricane Earl (2010) before and during rapid intensification. *Monthly Weather Review*, *146*(11), 3545–3565. https://doi.org/10.1175/MWR-D-18-0090.1

Wong, M. L. M., & Chan, J. C. L. (2004). Tropical cyclone intensity in vertical wind shear. *Journal of the Atmospheric Sciences*, *61*(15), 1859–1876. https://doi.org/10.1175/1520-0469(2004)061%3C1859:TCIIVW%3E2.0.CO;2

Yan, Y., Li, L., & Wang, C. (2017). The effects of oceanic barrier layer on the upper ocean response to tropical cyclones. *Journal of Geophysical Research: Oceans*, *122*, 4829–4844. https://doi.org/10.1002/2017JC012694

Zawislak, J., Jiang, H., Alvey, G. R., Zipser, E. J., Rogers, R. F., Zhang, J. A., & Stevenson, S. N. (2016). Observations of the structure and evolution of Hurricane Edouard (2014) during intensity change. Part I: Relationship between the thermodynamic structure and precipitation. *Monthly Weather Review*, *144*(9), 3333–3354. https://doi.org/10.1175/MWR-D-16-0018.1

Zhang, F., & Emanuel, K. (2016). On the role of surface fluxes and WISHE in tropical cyclone intensification. *Journal of the Atmospheric Sciences*, *73*(5), 2011–2019. https://doi.org/10.1175/JAS-D-16-0011.1

Zhang, J. A., Cione, J. J., Kalina, E. A., Uhlhorn, E. W., Hock, T., & Smith, J. A. (2017). Observations of infrared sea surface temperature and air-sea interaction in Hurricane Edouard (2014) using GPS dropsondes. *Journal of Atmospheric and Oceanic Technology*, *34*(6), 1333–1349. https://doi.org/10.1175/JTECH-D-16-0211

Zhang, J. A., Rogers, R. F., Nolan, D. S., & Marks, F. D. (2011). On the characteristic height scales of the hurricane boundary layer. *Monthly Weather Review*, *139*(8), 2523–2535. https://doi.org/10.1175/MWR-D-10-05017.1

Zhang, J. A., Rogers, R. F., Reasor, P. D., Uhlhorn, E. W., & Marks, F. D. (2013). Asymmetric hurricane boundary layer structure from dropsonde composites in relation to the environmental vertical wind shear. *Monthly Weather Review*, *141*(11), 3968–3984. https://doi.org/10.1175/MWR-D-12-00335.1

Zweng, M. M., Reagan, J. R., Antonov, J. I., Locarnini, R. A., Mishonov, A. V., Boyer, T. P., et al. (2013). In S. Levitus & A. Mishonov (Eds.), *World Ocean Atlas 2013, Volume 2: Salinity* (Vol. 74, pp. 1–39). NESDIS: NOAA Atlas.

Erratum

In the originally published version of this article, a typesetting error caused Figure 5 to publish as Figure 6, Figure 6 to publish as Figure 7, and Figure 7 to publish as Figure 5. The figures have since been corrected, and this version may be considered the authoritative version of record.